Development and validation of Navier–Stokes characteristic boundary conditions applied to turbomachinery simulations using the lattice Boltzmann method

Thomas Gianoli, Jean-françois Boussuge, Pierre Sagaut, Jérôme de Laborderie

Received: 19 April 2022 | Revised: 31 August 2022 | Accepted: 27 September 2022

DOI: 10.1002/fld.5160

RESEARCH ARTICLE

WILEY

Development and validation of Navier–Stokes characteristic boundary conditions applied to turbomachinery simulations using the lattice Boltzmann method

Thomas Gianoli[1,2,3] | **Jean-François Boussuge**[1] | **Pierre Sagaut**[2] | **Jérôme de Laborderie**[3]

[1]CERFACS, Toulouse Cedex, France

[2]M2P2, Aix Marseille Univ, Centrale Marseille, CNRS, M2P2 UMR 7340, Marseille Cedex, France

[3]Safran Aircraft Engines, Moissy-Cramayel, France

Correspondence
Thomas Gianoli, CERFACS, 42 Avenue G. Coriolis, 31057 Toulouse Cedex, France.
Email: thomas.gianoli-guillerme@safrangroup.com

Funding information
Safran Aircraft Engines; ANRT/CIFRE, Grant/Award Number: 2019/1448

Abstract

This article reports a procedure to implement as well as to validate non-reflecting boundary conditions applied for turbomachinery simulations, using Navier–Stokes characteristic boundary conditions in a compressible lattice Boltzmann solver. The implementation of both an inlet condition imposing total pressure, total temperature, and flow angles, as well as an outlet condition imposing a static pressure profile that allows the simulation to reach a simplified radial equilibrium, is described within the context of a lattice Boltzmann approach. The treatment at the boundaries relies on the characteristic methodology to derive conditions which are non-reflecting in terms of acoustics and is also compatible with turbulence injection at the inlet. These properties are evaluated on test cases of increasing complexity, ranging from a simple 2D periodic domain to an S-duct stage with turbulence injection.

KEYWORDS

characteristic boundary conditions, lattice Boltzmann method, LODI, turbomachinery

1 | INTRODUCTION

To design innovative engines for modern aircraft, the study of unsteady turbulent phenomena is required. However, turbulence prediction reveals to be a major issue, especially considering the complexity of the geometry involved. Thus, it remains a challenge to simulate the flow developing in modern aero-engines. Reynolds averaged Navier–Stokes (RANS) approaches, which model all the turbulent motions within the flow, remain the most widespread family of methods for turbomachinery simulations. However, these approaches often produce inaccurate results, and with the continuous increase in computing power, large eddy simulation (LES), which resolves the large scale turbulent motions, has become an increasingly appealing choice. However, the high computational cost of LES has limited its adoption in industrial CFD.

Considering these challenges, the lattice Boltzmann approach[1-3] has emerged in the fluid dynamics community as a viable method to solve the Navier–Stokes equations. The LBM has demonstrated its capability to handle complex geometries by the use of Cartesian grids, thanks to immersed boundary conditions.[4-7] Moreover, the low dissipation properties demonstrated by the LBM allow it to capture the small acoustic pressure fluctuations.[8,9] All these properties have attracted intensive research in aerodynamics,[10-12] aero-acoustics,[13] extension to weakly compressible thermal flows,[14-16] compressible flows,[17-21] and turbulent applications.[22-24] Finally, the algorithm of the method is well adapted to high-performance computing thanks to an easy parallelization.[25]

However, specifying inlet and outlet boundary conditions for compressible flow simulations remains a major issue, especially when wave reflections must be controlled.[26-28] For Navier–Stokes methods, a successful approach is the use of non-reflective boundary conditions based on a treatment of the characteristic waves of the local flow. The extension to the LBM framework is not straightforward considering that the LBM describes the population of particles at the mesoscopic level whereas the Navier–Stokes description applies at the macroscopic level.

Indeed, in practice, imposing an outlet boundary that is realistic and non-disturbing is a major issue in most cases. For an outlet condition to be considered ideal, it should have a weak influence on the upstream flow, remain stable, and minimize the reflection and dissipation of acoustic waves. These requirements become especially important when using LES or DNS which belong to the category of high-fidelity simulations. The principle of such methods is to resolve all or a part of the turbulence scales in highly turbulent and unsteady flows. Thus, the boundary should not create spurious reflections or acoustic waves inside the domain that would deteriorate the solution. In the particular case of turbomachinery flows, strong inhomogeneities are found at the stage exit in the form of wake effects, unsteady flow bubbles or pressure gradients. Moreover, the presence of blades and rotating parts create a flow deviation in the form of a swirling motion of the mean flow. This swirling motion generates a positive radial pressure gradient that is in equilibrium with the square of the tangential velocity. This so called radial equilibrium has to thus be satisfied by the static pressure profile imposed at the outlet condition. For (U)RANS simulations, it is usual for turbomachinery simulations to impose a static pressure profile that satisfies a simplified radial equilibrium. However, this methodology leads to a boundary which is not appropriate for proper LES and DNS as it is fully reflecting. It will be demonstrated that the NSCBC methodology applied at the outlet remains fully compatible with the need to verify the radial equilibrium while also being non-reflective.[29]

For the particular case of inlet boundary conditions in the turbomachinery field, the imposed values are usually expressed in terms of total pressure $P_t = P_s\left(1+\frac{\gamma-1}{2}Ma^2\right)^{\frac{\gamma}{\gamma-1}}$ and total temperature $T_t = T_s\left(1+\frac{\gamma-1}{2}Ma^2\right)$[30] where P_s represents the static pressure, T_s the static temperature. Furthermore, the flow direction, determined by the angles ϕ and α must also be specified (see Figure 4). Indeed, these quantities are commonly measured at different sections in an experimental facility using Pitot tubes and thermocouples. Once the total quantities are adequately imposed at the inlet, it must also be able to handle synthetic turbulence injection. Indeed, turbulence may have a major effect on the flow developing in a turbomachine.[31-36]

Finally, some recent progress has been made on the adaptation of characteristic boundary conditions to the LBM formalism. Their use has been extended to high Reynolds number flows using a regularized approach.[37] Moreover, an open boundary condition have been developed[38] using the LODI formalism coupled with a hybrid recursive regularized lattice Boltzmann method suited for compressible flow.

The goal of this article is to detail and validate an NSCBC methodology in a compressible LBM framework that is applicable to turbomachinery flows. This consists of the imposition of total pressure, total temperature, and flow direction at the inlet, with the possibility of adding synthetic turbulence injection, together with the imposition of a pressure profile satisfying a simplified radial equilibrium at the outlet. This article is structured as follows: Section 2 recalls the main principles underlying the compressible LBM. This section is then supplemented by Section 2.5 that focuses on the treatment of the boundary with the LBM. Then, Section 3 describes the NSCBC formulation for this particular inlet condition while Sections 4 and 5 assess the NSCBC methodology for the inlet and outlet respectively on several academical test-cases. Finally, Section 6 shows the practical use of these boundary conditions on an industrial configuration that consists of studying an S-duct stage.

2 | ADAPTATION IN THE LATTICE BOLTZMANN METHOD

2.1 | Short lattice Boltzmann method introduction: Classical BGK collision operator

The lattice Boltzmann method aims at solving the Boltzmann equation through space, time, and particle velocity discretization to describe the evolution of the discrete particle distribution functions $f_i(x, t)$. To do so, a Cartesian grid is used to discretize space and time while the particle velocities are discretized on what is usually called a lattice. The lattice is

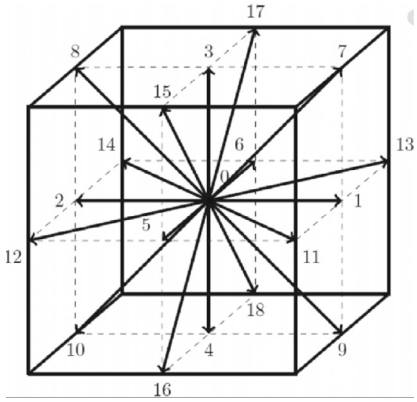

FIGURE 1 Scheme of the velocity directions for the D3Q19 lattice

described by its number of dimensions, denoted d, and the number q of discrete velocities $c_{i\alpha}$. The usual notation used to described the lattice is thus $DdQq$.

To solve the flow problem, it is necessary to obtain the density distribution function of particles with velocity $c_{i\alpha}$ located at (x_α, t) at the next time step $t + \Delta t$. The collision step is expressed using Equation (1). The collision operator $\Omega_i(x_\alpha, t)$ is approximated by the single-relaxation time Bhatnagar–Gross–Krook (Equation 2) model.[1,39]

$$f_i(x_\alpha + c_{i\alpha}\Delta t, t + \Delta t) - f_i(x_\alpha, t) = \Omega_i(x_\alpha, t) + \Psi_i, \tag{1}$$

$$\Omega_i(x_\alpha, t)^{(\mathrm{BGK})} = -\frac{1}{\tau}\left(f_i(x_\alpha, t) - f_i^{(\mathrm{eq})}(x_\alpha, t)\right), \tag{2}$$

where τ represents the relaxation time toward the equilibrium distribution function $f_i^{(\mathrm{eq})}(x_\alpha, t)$ and Ψ_i is a force term. This equilibrium distribution function is usually approximated using a development in the Hermite polynomials basis to an order N, $\mathcal{H}_i^{(n)}$.

$$f_i^{(\mathrm{eq})}(x_\alpha, t) = \omega_i \sum_{n=0}^{N} \frac{1}{c_s^{2n}!} \boldsymbol{a}_0^n : \mathcal{H}_i^{(n)}, \tag{3}$$

with c_s the lattice speed of sound and ω_i the Gaussian weights, which are characteristics of the set of velocities $c_{i\alpha}$ used to form the lattice. $\boldsymbol{a}_0^n$ are equilibrium coefficients recovered from a projection of the Maxwell–Boltzmann distribution function onto the Hermite polynomials base $\mathcal{H}_i^{(n)}$ expressed as

$$\mathcal{H}_i^{(n)} = \frac{(-c_s^2)^n}{\omega(c_i)} \nabla_c^n \omega(c_i). \tag{4}$$

In this article, the D3Q19 lattice (see Figure 1) is used, which leads to the following discrete velocities and weights:

$$[c_{i\alpha}, w_i] = \begin{cases} [(0,0,0), 1/3], & i = 0, \\ [(\pm 1, 0, 0), (0, \pm 1, 0), (0, 0, \pm 1), 1/18], & i = 1-6, \\ [(\pm 1, \pm 1, 0), (\pm 1, 0, \pm 1), (0, \pm 1, \pm 1), 1/36], & i = 7-18. \end{cases} \tag{5}$$

The macroscopic density ρ, and momentum ρu_α, with the general forcing term ψ_i are then deduced using:

$$\rho = \sum_i f_i, \tag{6}$$

$$\rho u_\alpha = \sum_i c_{i\alpha} f_i + \frac{\Delta t}{2} \sum_i c_{i\alpha} \psi_i. \tag{7}$$

Finally, a Chapman–Enskog expansion derives the link between the relaxation time τ, and the dimensionless kinematic viscosity ν. Using a BGK collision operator, this gives

$$\nu = c_s^2 \left(\tau - \frac{\Delta t}{2} \right). \tag{8}$$

However, it has been shown in the literature[40] that this choice of collision model lacks stability and is limited to the simulation of incompressible, athermal flows.[2,41,42] To overcome these issues, several methods have been investigated. For instance, the use of multiple relaxation times (MRT) model[43] allows to relax each moment of the distribution function at a specific relaxation rate, increasing the stability. Another method consists of building more advanced collision models, called regularized collision models, that cancel high-order contributions. This category of models has been shown to filter some non-hydrodynamic modes out of a computation and that they can be interpreted within the framework of entropic LBM, thus leading to thermal and compressible simulations.[38,39,44-51]

2.2 | Hybrid recursive regularized collision model

The lattice Boltzmann solver described in this section refers to the one used in all the presented simulations. The solver corresponds to a hybrid recursive regularized model[47] onto which the latest improvements described in the literature[52,53] are applied. The main modifications are the addition of a correction in all directions, leading to a more symmetric behavior, the reconstruction of the non-equilibrium distribution functions is encapsulated in lattice space and finally, the hybrid procedure does not longer depend on a tuning parameter.

The algorithm for the compressible lattice Boltzmann method with hybrid recursive regularization remains under the common form of collide and stream algorithm. The lattice Boltzmann BGK equation with hybrid recursive regularization is expressed[49] using Equation (9)

$$f_i(x_\alpha + c_{i\alpha}\Delta t, t + \Delta t) = f_i^{\mathrm{eq}}(x_\alpha, t) + \left(1 - \frac{1}{\tau}\right) \mathcal{R}(f_i^{\mathrm{neq}}) + \frac{\Delta t}{2}\psi_i(x_\alpha, t), \tag{9}$$

where τ is the relaxation time and $\mathcal{R}(\overline{f_i^{\mathrm{neq}}})$ is the hybrid recursive regularization on the off-equilibrium distribution function. This term is used to filter non-physical modes and is defined in the next section by Equation (12). $\psi(x_\alpha, t)$ is a forcing term meant to correct errors that are introduced by the D3Q19 lattice as well as other errors introduced by f_i^{eq} as detailed in the next section. The off-equilibrium distribution function is defined as:

$$f_i^{\mathrm{neq}} = f_i(x_\alpha, t) - f_i^{\mathrm{eq}}(x_\alpha, t) + \frac{\Delta t}{2}\psi_i(x_\alpha, t). \tag{10}$$

2.3 | Improved density-based approach and isotropic equilibrium

The goal of Equation (9) is to retrieve the physics of the fully compressible Navier–Stokes equations for a gas respecting the ideal gas law. To do so, an expression of f_i^{eq} and ψ_i must be set. Here, the formulation[53] is chosen with a modification on the second order terms[54] to obtain a better isotropy. The Gauss–Hermite polynomials used read:

$$\begin{aligned} \mathcal{H}_{i\alpha\beta}^{(2)} &= c_{i\alpha}c_{i\beta} - c_s^2\delta_{\alpha\beta}, \\ \mathcal{H}_{i\alpha\beta\gamma}^{(3)} &= c_{i\alpha}c_{i\beta}c_{i\gamma} - c_s^2(c_{i\alpha}\delta_{\beta\gamma} + c_{i\beta}\delta_{\gamma\alpha} + c_{i\gamma}\delta_{\alpha\beta}). \end{aligned} \tag{11}$$

Having defined theses polynomials, the hybrid recursive regularization on the off-equilibrium distribution function reads:

$$\mathcal{R}(f_i^{\mathrm{neq}}) = \omega_i \left[\frac{\mathcal{H}_{i\alpha\beta}^{(2)}}{2c_s^4}\mathcal{A}_{\alpha\beta}^{(1,\mathrm{HRR})} + \frac{\mathcal{H}_{i\alpha\beta\gamma}^{(3)}}{6c_s^6}\mathcal{A}_{\alpha\beta\gamma}^{(1,\mathrm{HRR})} \right], \tag{12}$$

with $\mathcal{A}^{(1)}_{\alpha\beta} = \sum_i c_{i\alpha} c_{i\beta} f_i^{\text{neq}}$ the second-order off-equilibrium moment, and the third-order moment is recursively computed using $\mathcal{A}^{(1)}_{\alpha\beta\gamma} = u_\alpha \mathcal{A}^{(1)}_{\beta\gamma} + u_\beta \mathcal{A}^{(1)}_{\gamma\alpha} + u_\gamma \mathcal{A}^{(1)}_{\alpha\beta}$. The equilibrium function is expressed depending on the zeroth to third order moments:

$$f_i^{\text{eq}} = \omega_i \rho (f_i^{\text{eq},(0)} + f_i^{\text{eq},(1)} + f_i^{\text{eq},(2)} + f_i^{\text{eq},(3)}). \tag{13}$$

The zeroth order moment contains the thermal information and ensures the coupling of the LBM solver with the ideal gas law:

$$f_i^{eq,0} = 1 + d_i, \quad \text{where } d_i = \begin{cases} \frac{\omega_0 - 1}{\omega_0}(\theta - 1), & \boldsymbol{c}_i = (0,0,0), \\ \theta - 1, & \text{else}, \end{cases} \tag{14}$$

where $\theta = rT/c_s^2$. The first order moment is identical to classic LBM approaches with

$$f_i^{\text{eq},(1)} = \frac{c_{i\alpha}}{c_s^2} u_\alpha. \tag{15}$$

Then, the second order moment is modified to account for isotropic improvements:[54]

$$f_i^{eq,2} = \begin{cases} -u_\alpha u_\alpha, & c_i = (0,0,0), \\ -3u_\alpha u_\alpha + 6(c_{i\alpha} u_\alpha)^2, & \boldsymbol{c}_i \in \{(\pm 1,0,0),(0,\pm 1,0),(0,0,\pm 1)\}, \\ -\frac{3}{2} c_{i\alpha}^2 u_\alpha^2 + \frac{9}{2}(c_{i\alpha} u_\alpha)^2, & \text{else}. \end{cases} \tag{16}$$

Finally, the third order moment is:

$$\begin{aligned} f_i^{eq,3} = \frac{1}{6c_s^2} \Big[& 3\left(\mathscr{H}^{(3)}_{ixxy} + \mathscr{H}^{(3)}_{iyzz}\right)\left(u_x u_x u_y + u_y u_z u_z\right) \\ & + \left(\mathscr{H}^{(3)}_{ixxy} - \mathscr{H}^{(3)}_{iyzz}\right)\left(u_x u_x u_y - u_y u_z u_z\right) \\ & + 3\left(\mathscr{H}^{(3)}_{ixzz} + \mathscr{H}^{(3)}_{ixyy}\right)\left(u_x u_z u_z + u_x u_y u_y\right) \\ & + \left(\mathscr{H}^{(3)}_{ixzz} - \mathscr{H}^{(3)}_{ixyy}\right)\left(u_x u_z u_z - u_x u_y u_y\right) \\ & + 3\left(\mathscr{H}^{(3)}_{iyyz} + \mathscr{H}^{(3)}_{ixxz}\right)\left(u_y u_y u_z + u_x u_x u_z\right) \\ & + \left(\mathscr{H}^{(3)}_{iyyz} - \mathscr{H}^{(3)}_{ixxz}\right)\left(u_y u_y u_z - u_x u_x u_z\right) \Big]. \end{aligned} \tag{17}$$

From this formulation of f_i^{eq}, as well as the limited number of discrete velocities with the D3Q19 lattice, this leads to errors in the viscous stress tensor such as the $\mathcal{O}(Ma^3)$ error. To correct these errors, the forcing terms ψ_i is written as:

$$\psi_i = -\omega_i \frac{\mathcal{H}^{(2)}_{i\alpha\beta}}{2c_s^4} \Psi_{\alpha\beta}, \tag{18}$$

with $\Psi_{\alpha\beta}$ defined as:

$$\begin{aligned} \Psi_{\alpha\beta} = & c_s^2 u_\alpha \frac{\partial(\rho(1-\theta))}{\partial x_\beta} + c_s^2 u_\beta \frac{\partial(\rho(1-\theta))}{\partial x_\alpha} \\ & + \frac{2}{3}\delta_{\alpha\beta}\rho c_s^2 \frac{\partial u_\gamma}{\partial x_\gamma} - \delta_{\alpha\beta} c_s^2 \frac{\partial \rho(1-\theta)}{\partial t} + \frac{\partial Err_{\alpha\beta\gamma}}{\partial x_\gamma}. \end{aligned} \tag{19}$$

The terms in Equation (19) are discretized using a standard second-order centered scheme. A Chapman–Enskog expansion[55] shows that Equation (9) with the equilibrium distribution (Equation 15) and the correction terms (Equation 19) allows to retrieve the compressible Navier–Stokes equations.

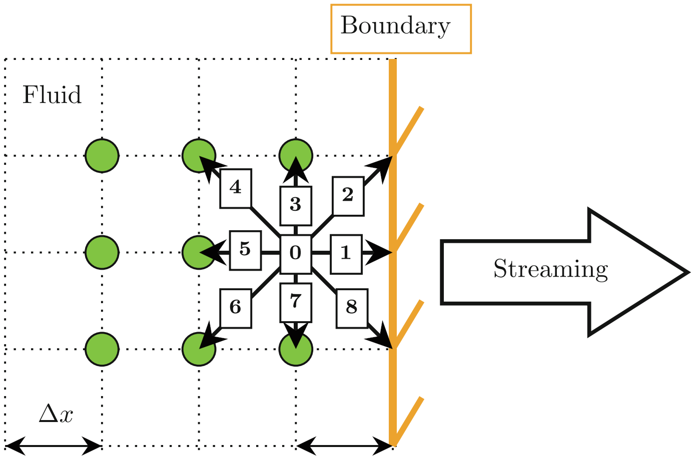

FIGURE 2 Issue at a boundary node illustrated on a D2Q9 lattice. The unknown populations are represented by the red dashed arrows. [Colour figure can be viewed at wileyonlinelibrary.com]

2.4 | Energy conservation using entropy equation

For the hybrid compressible lattice Boltzmann method discussed above, the strategy of hybridization[50] consists of using a non-conservative form of the entropy conservation equation with the corresponding expression:

$$\frac{\partial s}{\partial t} + u_\alpha \frac{\partial s}{\partial x_\alpha} = \frac{1}{\rho T}\frac{\partial s}{\partial x_\alpha}\left(\lambda \frac{\partial T}{\partial x_\alpha}\right) + \frac{1}{\rho T}\Pi_{\alpha\beta}\frac{\partial u_\alpha}{\partial x_\beta}, \tag{20}$$

where $s = c_v \ln(\frac{P}{\rho^\gamma})$ is the entropy, λ is the heat conductivity, and $\Pi_{\alpha\beta}$ is the viscous stress tensor. The temporal integration is achieved using an explicit Euler scheme. The convective flux is then obtained using third-order MUSCL scheme[56] and the van Albada limiter,[57] while the diffusion term and the viscous dissipation are approached using a second-order central difference scheme.

2.5 | Adaptation with the regularized boundary condition

From the previous section, it should be noted that a problem appears at the boundary after the streaming step.[58,59] Indeed, on a boundary node, some populations are unknown before the collision since they are coming from outside the computational domain as illustrated in Figure 2.

A finite difference-based reconstruction is applied along with the hybrid regularization procedure[37,38,49,50,60-62] to compute the distribution functions at the boundary. The methodology is the following:

- The macroscopic values of ρ, u, P on the boundary nodes are prescribed based on an interpolation/extrapolation scheme through a cut-cell approach.[38]
- The entropy s and the temperature T_s can then be estimated thanks to the thermodynamic closure and equation of state.
- Then, using the velocity gradients, the shear stress tensor and correction term ψ are computed at the boundary node with a first order biased finite-difference scheme.
- Then the distribution functions are computed[38] such as $f_i = f_i^{\text{eq}} + f_i^{\text{neq}}$. The off-equilibrium distribution function f_i^{neq} is recursively reconstructed from the macroscopic variables and their gradients.

Thus $f_i^{\text{eq}}, f_i^{\text{neq}}, \psi$ are fully defined at the boundary node, and the recursive collision operation followed by the streaming step toward neighboring nodes in the fluid domain can be performed.

3 | THEORY OF THE NAVIER–STOKES CHARACTERISTIC BOUNDARY CONDITIONS

Starting from the Navier–Stokes equations, written using Einstein notation, for a compressible viscous flow, one has:

$$\frac{\partial \rho}{\partial t} + \frac{\partial m_i}{\partial x_i} = 0, \tag{21}$$

$$\frac{\partial m_i}{\partial t} + \frac{\partial m_i u_j}{\partial x_j} + \frac{\partial P_s}{\partial x_i} = \frac{\partial \tau_{ij}}{\partial x_j}, \tag{22}$$

$$\frac{\partial \rho E}{\partial t} + \frac{\partial (\rho E + P_s) u_i}{\partial x_i} = \frac{\partial u_i \tau_{ij}}{\partial x_i} - \frac{\partial q_i}{\partial x_i}, \tag{23}$$

with the corresponding notations

$$\rho E = \frac{1}{2} \rho u_k u_k + \frac{P_s}{\gamma - 1}, \tag{24}$$

$$m_i = \rho u_i, \tag{25}$$

where ρ is the local fluid density, u_i the velocity components, P_s the static pressure, T_s the static temperature, E the total energy, and τ_{ij} the stress tensor defined as:

$$\tau_{ij} = \mu \left(\frac{\partial u_i}{\partial x_j} + \frac{\partial u_j}{\partial x_i} - \frac{2}{3} \delta_{ij} \frac{\partial u_k}{\partial x_k} \right). \tag{26}$$

δ_{ij} is the Kronecker symbol and μ the dynamic viscosity. q_i is the heat flux along the x_i direction and is defined as $q_i = -\lambda \frac{\partial T_s}{\partial x_i}$, where λ is the thermal conductivity. The system is finally closed using the ideal gas law:

$$P_s = \rho r T_s, \tag{27}$$

where r is the specific constant of the mixture $r = \frac{R}{W}$, with W the mean molecular weight of the mixture and $R = 8.3143$ J/mol K is the universal gas constant.

Using characteristic analysis,[26,63,64] it is possible to transform the vector of conservatives variables $\boldsymbol{U} = (\rho, \rho u, \rho v, \rho w, \rho E)^T$ or the vector of primitive variables expressed in the reference frame $\vec{n}, \vec{t_1}, \vec{t_2}$ written $\boldsymbol{V} = (\rho, P_s, u_n, u_{t_1}, u_{t_2})^T$ into characteristic variables. To do so, the Navier–Stokes equations are written under matrix form:

$$\frac{\partial \boldsymbol{U}}{\partial t} + \boldsymbol{A_U} \frac{\partial \boldsymbol{U}}{\partial \boldsymbol{x}} + \boldsymbol{B_U} \frac{\partial \boldsymbol{U}}{\partial \boldsymbol{y}} + \boldsymbol{C_U} \frac{\partial \boldsymbol{U}}{\partial \boldsymbol{z}} + \boldsymbol{S} = \boldsymbol{0}, \tag{28}$$

where $\boldsymbol{A_U}$, $\boldsymbol{B_U}$, $\boldsymbol{C_U}$ are the Jacobian matrices of the respective fluxes in the x, y, z directions, and $\boldsymbol{S}$ is the diffusion term. In the same way, $\boldsymbol{V}$ verifies:

$$\frac{\partial \boldsymbol{V}}{\partial t} + \boldsymbol{N} \frac{\partial \boldsymbol{V}}{\partial \boldsymbol{n}} + \boldsymbol{T_1} \frac{\partial \boldsymbol{V}}{\partial \boldsymbol{t_1}} + \boldsymbol{T_2} \frac{\partial \boldsymbol{V}}{\partial \boldsymbol{t_2}} + \boldsymbol{S} = \boldsymbol{0}, \tag{29}$$

where $\boldsymbol{N}$ is the normal Jacobian, $\boldsymbol{T_1}$, $\boldsymbol{T_2}$ are the two tangential Jacobian along $\vec{t_1}$ and $\vec{t_2}$.

The fully developed primitives equations read:

$$\frac{\partial \rho}{\partial t} + u_n \frac{\partial \rho}{\partial n} + u_{t_1} \frac{\partial \rho}{\partial t_1} + u_{t_2} \frac{\partial \rho}{\partial t_2} + \rho \left(\frac{\partial u_n}{\partial n} + \frac{\partial u_{t_1}}{\partial t_1} + \frac{\partial u_{t_2}}{\partial t_2} \right) = 0, \tag{30}$$

$$\frac{\partial P_s}{\partial t} + u_n \frac{\partial P_s}{\partial n} + u_{t_1} \frac{\partial P_s}{\partial t_1} + u_{t_2} \frac{\partial P_s}{\partial t_2} + \gamma P_s \left(\frac{\partial u_n}{\partial n} + \frac{\partial u_{t_1}}{\partial t_1} + \frac{\partial u_{t_2}}{\partial t_2} \right) = 0, \tag{31}$$

$$\frac{\partial u_n}{\partial t} + u_n \frac{\partial u_n}{\partial n} + u_{t_1} \frac{\partial u_n}{\partial t_1} + u_{t_2} \frac{\partial u_n}{\partial t_2} + \frac{1}{\rho} \frac{\partial P_s}{\partial n} = 0, \tag{32}$$

$$\frac{\partial u_{t_1}}{\partial t} + u_n \frac{\partial u_{t_1}}{\partial n} + u_{t_1} \frac{\partial u_{t_1}}{\partial t_1} + u_{t_2} \frac{\partial u_{t_1}}{\partial t_2} + \frac{1}{\rho}\frac{\partial P_s}{\partial t_1} = 0, \tag{33}$$

$$\frac{\partial u_{t_2}}{\partial t} + u_n \frac{\partial u_{t_2}}{\partial n} + u_{t_1} \frac{\partial u_{t_2}}{\partial t_1} + u_{t_2} \frac{\partial u_{t_2}}{\partial t_2} + \frac{1}{\rho}\frac{\partial P_s}{\partial t_2} = 0. \tag{34}$$

Considering that the normal at the surface for the boundary is $\vec{n}$, the equations are written as:

$$\frac{\partial \boldsymbol{V}}{\partial t} + \boldsymbol{N}\frac{\partial \boldsymbol{V}}{\partial \boldsymbol{n}} + \boldsymbol{C} = \boldsymbol{0}. \tag{35}$$

With $\boldsymbol{N}$ expressed in Equation (36) and $\boldsymbol{C}$ is the vector containing all remaining terms which do not involve elements in the normal direction (terms of $\partial \boldsymbol{V}/\partial n$).

$$\boldsymbol{N} = \begin{pmatrix} u_n & 0 & \rho & 0 & 0 \\ 0 & u_n & \gamma P_s & 0 & 0 \\ 0 & 1/\rho & u_n & 0 & 0 \\ 0 & 0 & 0 & u_n & 0 \\ 0 & 0 & 0 & 0 & u_n \end{pmatrix}. \tag{36}$$

Considering that the speed of sound is $c^2 = \frac{\gamma P_s}{\rho}$, computing the eigenvalues λ_i of $\boldsymbol{N}$ yields the diagonal matrix D with the corresponding eigenvalues: $\lambda_1 = u_n - c$, $\lambda_2 = \lambda_3 = \lambda_4 = u_n$, and $\lambda_5 = u_n + c$.

$$\boldsymbol{D} = \begin{pmatrix} u_n - c & 0 & 0 & 0 & 0 \\ 0 & u_n & 0 & 0 & 0 \\ 0 & 0 & u_n & 0 & 0 \\ 0 & 0 & 0 & u_n & 0 \\ 0 & 0 & 0 & 0 & u_n + c \end{pmatrix}. \tag{37}$$

The corresponding eigenvectors are:

$$\boldsymbol{l_1^T} = (0, 1, -\rho c, 0, 0), \tag{38}$$

$$\boldsymbol{l_2^T} = (c^2, -1, 0, 0, 0), \tag{39}$$

$$\boldsymbol{l_3^T} = (0, 0, 0, 1, 0), \tag{40}$$

$$\boldsymbol{l_4^T} = (0, 0, 0, 0, 1), \tag{41}$$

$$\boldsymbol{l_5^T} = (0, 1, \rho c, 0, 0). \tag{42}$$

By inverting these definitions it is possible to write the normal derivative terms ($\partial \boldsymbol{V}/\partial n$):

$$\frac{\partial \rho}{\partial n} = \frac{1}{c^2}\left(\frac{\mathcal{L}_s}{u_n} + \frac{1}{2}\left[\frac{\mathcal{L}_+}{u_n + c} + \frac{\mathcal{L}_-}{u_n - c}\right]\right), \tag{43}$$

$$\frac{\partial P_s}{\partial n} = \frac{1}{2}\left(\frac{\mathcal{L}_+}{u_n + c} + \frac{\mathcal{L}_-}{u_n - c}\right), \tag{44}$$

$$\frac{\partial u_n}{\partial n} = \frac{1}{2\rho c}\left(\frac{\mathcal{L}_+}{u_n + c} - \frac{\mathcal{L}_-}{u_n - c}\right), \tag{45}$$

$$\frac{\partial u_{t_1}}{\partial n} = \frac{\mathcal{L}_{t_1}}{u_n}, \tag{46}$$

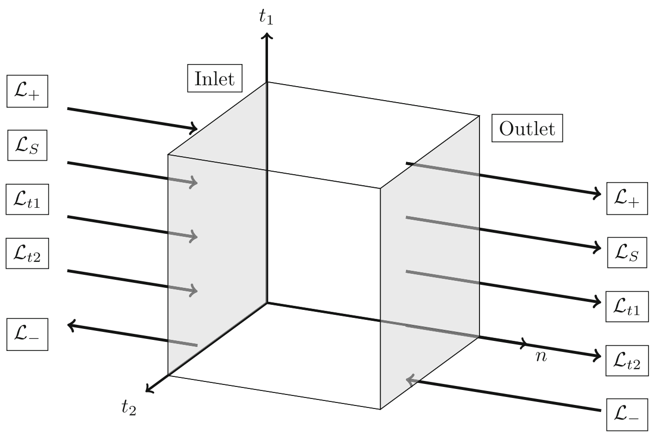

FIGURE 3 Representation of the $\mathcal{L}_i$ waves leaving or entering the computational domain

$$\frac{\partial u_{t_2}}{\partial n} = \frac{\mathcal{L}_{t_2}}{u_n}. \tag{47}$$

Then we substitute these expressions of $\partial \boldsymbol{V}/\partial n$ into the terms of $\boldsymbol{N}\partial \boldsymbol{V}/\partial n$ (Equations 30–34) leading to the following primitive equations:

$$\frac{\partial \rho}{\partial t} + \frac{1}{c^2}\left(\mathcal{L}_s + \frac{1}{2}[\mathcal{L}_+ + \mathcal{L}_-]\right) + u_{t_1}\frac{\partial \rho}{\partial t_1} + u_{t_2}\frac{\partial \rho}{\partial t_2} + \rho\left(\frac{\partial u_{t_1}}{\partial t_1} + \frac{\partial u_{t_2}}{\partial t_2}\right) = 0, \tag{48}$$

$$\frac{\partial P_s}{\partial t} + \frac{1}{2}(\mathcal{L}_+ + \mathcal{L}_-) + u_{t_1}\frac{\partial P_s}{\partial t_1} + u_{t_2}\frac{\partial P_s}{\partial t_2} + \gamma P_s\left(\frac{\partial u_{t_1}}{\partial t_1} + \frac{\partial u_{t_2}}{\partial t_2}\right) = 0, \tag{49}$$

$$\frac{\partial u_n}{\partial t} + \frac{1}{2\rho c}(\mathcal{L}_+ - \mathcal{L}_-) + u_{t_1}\frac{\partial u_n}{\partial t_1} + u_{t_2}\frac{\partial u_n}{\partial t_2} - g_n = 0, \tag{50}$$

$$\frac{\partial u_{t_1}}{\partial t} + \mathcal{L}_{t_1} + u_{t_1}\frac{\partial u_{t_1}}{\partial t_1} + u_{t_2}\frac{\partial u_{t_1}}{\partial t_2} + \frac{1}{\rho}\frac{\partial P_s}{\partial t_1} - g_{t_1} = 0, \tag{51}$$

$$\frac{\partial u_{t_2}}{\partial t} + \mathcal{L}_{t_2} + u_{t_1}\frac{\partial u_{t_2}}{\partial t_1} + u_{t_2}\frac{\partial u_{t_2}}{\partial t_2} + \frac{1}{\rho}\frac{\partial P_s}{\partial t_2} - g_{t_2} = 0. \tag{52}$$

The wave amplitude associated with each characteristic velocity λ_i is noted $\mathcal{L}_i = \lambda_i \frac{\partial \boldsymbol{W}}{\partial n}$, with i the index of the corresponding wave and $\boldsymbol{W}$ is the vector of characteristic variables. The characteristic analysis applied to the Navier–Stokes equations finally leads to the following expression for the characteristic waves $\mathcal{L}_i$ associated to the characteristic velocities, written in the local reference frame:

$$\begin{pmatrix} \mathcal{L}_+ \\ \mathcal{L}_- \\ \mathcal{L}_{t_1} \\ \mathcal{L}_{t_2} \\ \mathcal{L}_S \end{pmatrix} = \begin{pmatrix} (u_n + c)\left(\frac{\partial u_n}{\partial n} + \frac{1}{\rho c}\frac{\partial P_s}{\partial n}\right) \\ (u_n - c)\left(-\frac{\partial u_n}{\partial n} + \frac{1}{\rho c}\frac{\partial P_s}{\partial n}\right) \\ u_n \frac{\partial u_{t_1}}{\partial n} \\ u_n \frac{\partial u_{t_2}}{\partial n} \\ u_n\left(\frac{\partial \rho}{\partial n} - \frac{1}{c^2}\frac{\partial P_s}{\partial n}\right) \end{pmatrix}. \tag{53}$$

As illustrated in Figure 3, for an inlet, $\mathcal{L}_+$ and $\mathcal{L}_-$ are, respectively, the inward and outward acoustic waves, whereas $\mathcal{L}_{t_1}$ and $\mathcal{L}_{t_2}$ are transverse shear waves, and $\mathcal{L}_s$ is the entropic wave.

The NSCBC strategy used in this article is based on locally one-dimensional inviscid (LODI) flow on the boundary to specify the amplitude of ingoing waves. Under the LODI assumption, the characteristic system for the Navier–Stokes equations becomes:

$$\frac{\partial \rho}{\partial t} + \left(\mathcal{L}_S + \frac{\rho}{2c}(\mathcal{L}_+ + \mathcal{L}_-)\right) = 0, \tag{54}$$

$$\frac{\partial P_s}{\partial t} + \frac{\rho c}{2}(\mathcal{L}_+ + \mathcal{L}_-) = 0, \tag{55}$$

$$\frac{\partial T_s}{\partial t} + \frac{(\gamma-1)T_s}{2c}(\mathcal{L}_+ + \mathcal{L}_-) = 0, \tag{56}$$

$$\frac{\partial s}{\partial t} - \frac{c^2 \mathcal{L}_s}{(\gamma-1)\rho T} = 0, \tag{57}$$

$$\frac{\partial u_n}{\partial t} + \frac{1}{2}(\mathcal{L}_+ - \mathcal{L}_-) = 0, \tag{58}$$

$$\frac{\partial u_{t_1}}{\partial t} + \mathcal{L}_{t_1} = 0, \tag{59}$$

$$\frac{\partial u_{t_2}}{\partial t} + \mathcal{L}_{t_2} = 0. \tag{60}$$

It is necessary to specify the ingoing wave amplitudes to advance the solution in time at the boundary. It should also be noted that only one of the two equations (Equations 55 or 56) is needed thanks to the ideal gas law.

Some algebra is required to rewrite the LODI expressions using the P_t and T_t variables. This approach has been first presented by Odier et al.[30] and will be recalled here. First, they need to be expressed as functions of the local Mach number written Ma. Thus, to compute the time derivative of P_t and T_t, the time derivative of the Mach number is involved. However, it is possible to write the Mach number as a function of the kinetic energy e_c, the adiabatic coefficient γ, the specific gas constant r and the static temperature T_s according to Equation (61):

$$Ma^2 = \frac{u_n^2 + u_{t_1}^2 + u_{t_2}^2}{\gamma r T_s} = \frac{2e_c}{\gamma r T_s}. \tag{61}$$

However, the kinetic energy e_c is defined as:

$$e_c = \frac{u_n^2 + u_{t_1}^2 + u_{t_2}^2}{2}. \tag{62}$$

The kinetic energy temporal derivative is thus:

$$\frac{\partial e_c}{\partial t} = u_n \frac{\partial u_n}{\partial t} + u_{t_1}\frac{\partial u_{t_1}}{\partial t} + u_{t_2}\frac{\partial u_{t_2}}{\partial t}. \tag{63}$$

Using Equations (58)–(60), the temporal derivative of the kinetic energy can be written as:

$$\frac{\partial e_c}{\partial t} = -\frac{u_n}{2}(\mathcal{L}_+ - \mathcal{L}_-) + u_{t_1}\mathcal{L}_{t_1} + u_{t_2}\mathcal{L}_{t_2}. \tag{64}$$

The temporal derivative of the Mach number is expressed using Equation (64):

$$\frac{\partial Ma^2}{\partial t} = \frac{2}{c^2}\left(\mathcal{L}_+\left(\frac{(\gamma-1)e_c}{2c} - \frac{u_n}{2}\right) + \mathcal{L}_-\left(\frac{(\gamma-1)e_c}{2c} + \frac{u_n}{2}\right). - u_{t_1}\mathcal{L}_{t_1} - u_{t_2}\mathcal{L}_{t_2} - \frac{e_c}{2}\mathcal{L}_s\right). \tag{65}$$

Moreover, using the definition of the total pressure:

$$P_t = P_s\left(1 + \frac{(\gamma-1)}{2}Ma^2\right)^{\frac{\gamma}{(\gamma-1)}}. \tag{66}$$

The temporal derivative of the total pressure is:

$$\frac{\partial P_t}{\partial t} = \frac{\partial P_s}{\partial t}\left(1 + \frac{(\gamma-1)}{2}Ma^2\right)^{\frac{\gamma}{(\gamma-1)}} + \frac{P_s\gamma}{2}.\frac{\partial Ma^2}{\partial t}\left(1 + \frac{(\gamma-1)}{2}Ma^2\right)^{\frac{\gamma}{(\gamma-1)}-1}. \tag{67}$$

Using Equation (65) in Equation (67), the total pressure temporal derivative becomes:

$$\frac{\partial P_t}{\partial t} = \mathcal{L}_+ \left(-\frac{\rho c P_t}{2P_s} + \frac{P_t}{rT_t} \left(\frac{(\gamma-1)e_c}{2c} - \frac{u_n}{2} \right) \right) + \mathcal{L}_- \left(-\frac{\rho c P_t}{2P_s} + \frac{P_t}{rT_t} \left(\frac{(\gamma-1)e_c}{2c} + \frac{u_n}{2} \right) \right)$$
$$- \frac{P_t}{rT_t} \left(u_{t_1}\mathcal{L}_{t_1} + u_{t_2}\mathcal{L}_{t_2} + \frac{e_c}{\rho}\mathcal{L}_s \right). \tag{68}$$

With the same method, starting from the definition of the total temperature:

$$T_t = T_s \left(1 + \frac{(\gamma-1)}{2} Ma^2 \right). \tag{69}$$

The temporal derivative of the total temperature is:

$$\frac{\partial T_t}{\partial t} = \frac{\partial T_s}{\partial t} \frac{T_t}{T_s} + T_s \frac{(\gamma-1)}{2} \frac{\partial Ma^2}{\partial t}. \tag{70}$$

Then using Equations (56) and (65):

$$\frac{\partial T_t}{\partial t} = \mathcal{L}_+ \left(-\frac{(\gamma-1)T_t}{2c} + \frac{1}{C_p} \left(\frac{(\gamma-1)e_c}{2c} - \frac{u_n}{2} \right) \right) + \mathcal{L}_- \left(-\frac{(\gamma-1)T_t}{2c} + \frac{1}{C_p} \left(\frac{(\gamma-1)e_c}{2c} + \frac{u_n}{2} \right) \right)$$
$$- \frac{1}{C_p} \left(u_{t_1}\mathcal{L}_{t_1} + u_{t_2}\mathcal{L}_{t_2} + \frac{e_c}{\rho}\mathcal{L}_s \right). \tag{71}$$

With C_p being the specific heat ratio:

$$Cp = \frac{\gamma r}{\gamma - 1}. \tag{72}$$

The flow direction is fixed by choosing a flow angle ϕ and α (see Figure 4). Then, $\sin(\phi)$ and $\sin(\alpha)$ can be linked to the local flow velocity vector with:

$$\sin(\phi) = \frac{u_{t_1}}{\left\| \vec{U} \right\|}, \tag{73}$$

$$\sin(\alpha) = \frac{u_{t_2}}{\left\| \vec{U} \right\|}, \tag{74}$$

$$\text{with} \quad \left\| \vec{U} \right\| = \sqrt{u_n^2 + u_{t_1}^2 + u_{t_2}^2}. \tag{75}$$

The last step consists in determining the wave expressions of $\mathcal{L}_+$ and $\mathcal{L}_s$ by solving the system constituted by Equations (68) and (71):

$$\mathcal{L}_+ \left(-\frac{\rho c P_t}{2P_s} + \frac{P_t}{rT_t} \left(\frac{(\gamma-1)e_c}{2c} - \frac{u_n}{2} \right) \right) - \frac{e_c P_t}{\rho r T_t}\mathcal{L}_s = \frac{\partial P_t}{\partial t} - \mathcal{L}_- \left(-\frac{\rho c P_t}{2P_s} + \frac{P_t}{rT_t} \left(\frac{(\gamma-1)e_c}{2c} + \frac{u_n}{2} \right) \right)$$
$$+ \frac{P_t}{rT_t} \left(u_{t_1}\mathcal{L}_{t_1} + u_{t_2}\mathcal{L}_{t_2} \right), \tag{76}$$

$$\mathcal{L}_+ \left(-\frac{(\gamma-1)T_t}{2c} + \frac{1}{C_p} \left(\frac{(\gamma-1)e_c}{2c} - \frac{u_n}{2} \right) \right) - \frac{e_c}{\rho C_p}\mathcal{L}_s = \frac{\partial T_t}{\partial t} - \mathcal{L}_- \left(-\frac{(\gamma-1)T_t}{2c} + \frac{1}{C_p} \left(\frac{(\gamma-1)e_c}{2c} + \frac{u_n}{2} \right) \right)$$
$$+ \frac{1}{C_p} \left(u_{t_1}\mathcal{L}_{t_1} + u_{t_2}\mathcal{L}_{t_2} \right), \tag{77}$$

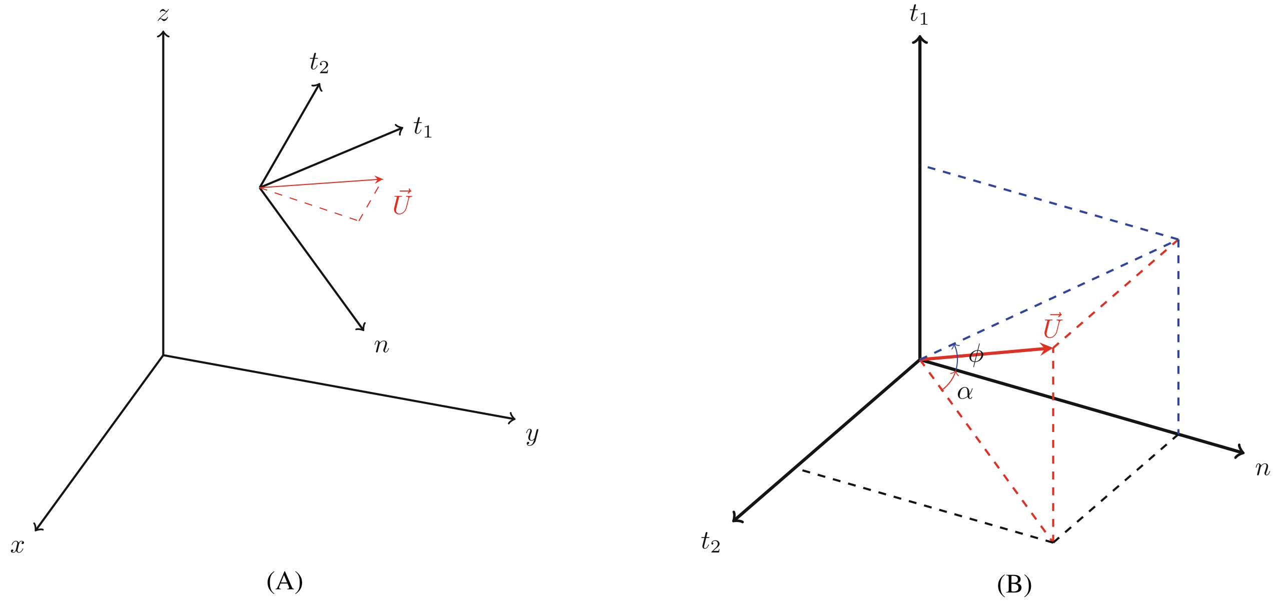

FIGURE 4 (A) Rotation from Cartesian basis to normal patch. (B) Flow direction angles ϕ, α associated to the velocity vector $\vec{U}$ [Colour figure can be viewed at wileyonlinelibrary.com]

$$
\begin{cases}
\mathcal{L}_+ F_4 - \mathcal{L}_s.F_1 = \dfrac{\partial P_t}{\partial t} + \dfrac{P_t}{rT_t}.F_3 - \mathcal{L}_-.F_6, & (78)\\[2ex]
\mathcal{L}_+ F_4 - \mathcal{L}_s.F_1 = \dfrac{\partial P_t}{\partial t} + \dfrac{P_t}{rT_t}.F_3 - \mathcal{L}_-.F_6. & (79)
\end{cases}
$$

Combining Equation (78) $\times F_2$ and adding Equation (79) $\times F_1$ gives:

$$\mathcal{L}_+ (F_4F_2 + F_5F_1) = F_2\frac{\partial P_t}{\partial t} + F_1\frac{\partial T_t}{\partial t} + \frac{P_t}{rT_t}F_3F_2 + \frac{F_3F_1}{C_p} - \mathcal{L}_-(F_6F_2 + F_1F_7). \tag{80}$$

Finally, $\mathcal{L}_+$ can be extracted from Equation (80) and gives Equation (84). Once $\mathcal{L}_+$ has been expressed, the unknown $\mathcal{L}_S$ wave is deduced from Equation (79) giving Equation (85).

Solving this system allows to write the following expressions for the wave amplitudes:

$$\mathcal{L}_- = (u_n - c)\left(-\frac{\partial u_n}{\partial n} + \frac{1}{\rho c}\frac{\partial P_s}{\partial n}\right), \tag{81}$$

$$\mathcal{L}_{t_1} = -\frac{\partial u_{t_1}}{\partial t}, \tag{82}$$

$$\mathcal{L}_{t_2} = -\frac{\partial u_{t_2}}{\partial t}, \tag{83}$$

$$\mathcal{L}_+ = \frac{F_1\frac{\partial T_t}{\partial t} + F_2\frac{\partial P_t}{\partial t} + F_1F_3\frac{P_t}{rT_t} - (F_2F_6 + F_1F_7)\mathcal{L}_-}{F_4F_2 + F_5F_1}, \tag{84}$$

$$\mathcal{L}_S = \frac{\frac{\partial T_t}{\partial t} + F_3\frac{1}{C_p} - F_5\mathcal{L}_+ - F_7\mathcal{L}_-}{F_2}. \tag{85}$$

With the following useful relations:

$$e_c = \frac{u_n^2 + u_{t_1}^2 + u_{t_2}^2}{2}, \tag{86}$$

$$F1 = \frac{e_c P_t}{\rho r T_t}, \tag{87}$$

$$F2 = \frac{T_t}{\rho} - \frac{e_c}{\rho C_p}, \tag{88}$$

$$F3 = \mathcal{L}_{t_1} u_{t_1} + \mathcal{L}_{t_2} u_{t_2}, \tag{89}$$

$$F4 = -\frac{\rho c P_t}{2P_s} + \frac{P_t}{rT_t}\left(\frac{(\gamma-1)e_c}{2c} - \frac{u_n}{2}\right), \tag{90}$$

$$F5 = -\frac{(\gamma-1)T_t}{2c} + \frac{1}{C_p}\left(\frac{(\gamma-1)e_c}{2c} - \frac{u_n}{2}\right), \tag{91}$$

$$F6 = -\frac{\rho c P_t}{2P_s} + \frac{P_t}{rT_t}\left(\frac{(\gamma-1)e_c}{2c} + \frac{u_n}{2}\right), \tag{92}$$

$$F7 = -\frac{(\gamma-1)T_t}{2c} + \frac{1}{C_p}\left(\frac{(\gamma-1)e_c}{2c} + \frac{u_n}{2}\right). \tag{93}$$

$\mathcal{L}_+$ is dependent of $\mathcal{L}_-$ which implies reflection for acoustics. To ensure non-reflectivity $\mathcal{L}_-$ is set to 0 which simplifies Equations (84) and (85). The wave amplitudes are finally written:

$$\mathcal{L}_- = (u_n - c)\left(-\frac{\partial u_n}{\partial n} + \frac{1}{\rho c}\frac{\partial P_s}{\partial n}\right), \tag{94}$$

$$\mathcal{L}_{t_1} = -\frac{\partial u_{t_1}}{\partial t}, \tag{95}$$

$$\mathcal{L}_{t_2} = -\frac{\partial u_{t_2}}{\partial t}, \tag{96}$$

$$\mathcal{L}_+ = \frac{F_1 \frac{\partial T_t}{\partial t} + F_2 \frac{\partial P_t}{\partial t} + F_1 F_3 \frac{P_t}{rT_t}}{F_4 F_2 + F_5 F_1}, \tag{97}$$

$$\mathcal{L}_S = \frac{\frac{\partial T_t}{\partial t} + F_3 \frac{1}{C_p} - F_5 \mathcal{L}_+}{F_2}. \tag{98}$$

To avoid a drift between the computed and the target value, a linear relaxation method[65] is used as detailed below:

$$\frac{\partial X}{\partial t} dt = -\sigma_X (X_{\text{predicted}} - X_{\text{target}}), \tag{99}$$

where σ_X is an user-chosen relaxation coefficient (same for every variable), $X_{\text{predicted}}$ is the value predicted by the numerical scheme and X_{target} is the value imposed at the boundary. These evaluations are used in Equations (82–(85) with X being $\sin(\phi)$, $\sin(\alpha)$, P_t, T_t. If σ_X is different from 0 the condition is partially non reflective. The consequences of such a relaxation method[66] will be studied later in this article.

4 | VALIDATION OF THE NSCBC INLET

4.1 | Convergence toward the mean values

The goal of this first simplified 2D test-case is to validate the implementation of the inlet boundary condition. This test case is built similarly to a previous study performed with the compressible LES solver AVBP[30] to be able to compare the results. It is built as a square of dimension $[L_x \times L_y] = [100 \text{ mm} \times 100 \text{ mm}]$ discretized with $[n_x \times n_y] = [128 \times 128]$ cells (see Figure 5). The minimal mesh size chosen imposes a time step $\Delta t = 1.33 \times 10^{-6}$ s. The inlet condition is set to inject air with a total pressure $P_t = 9.8803 \times 10^4$ Pa, a total temperature $T_t = 281$ K and a normal flow direction ($\alpha = \phi = 0°$). The kinematic viscosity is set to 1.397×10^{-5} m^2 s^{-1} corresponding to air at this temperature. The outlet condition is imposed as an outflow boundary with a static pressure $P_s = 7.1 \times 10^4$ Pa. On the other boundaries, periodic conditions are applied.

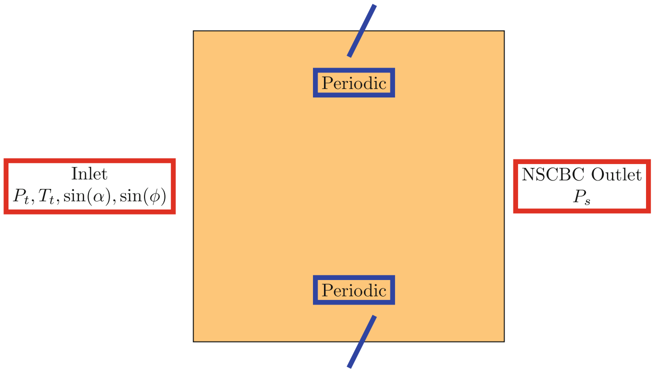

FIGURE 5 Scheme of the 2D square box test case [Colour figure can be viewed at wileyonlinelibrary.com]

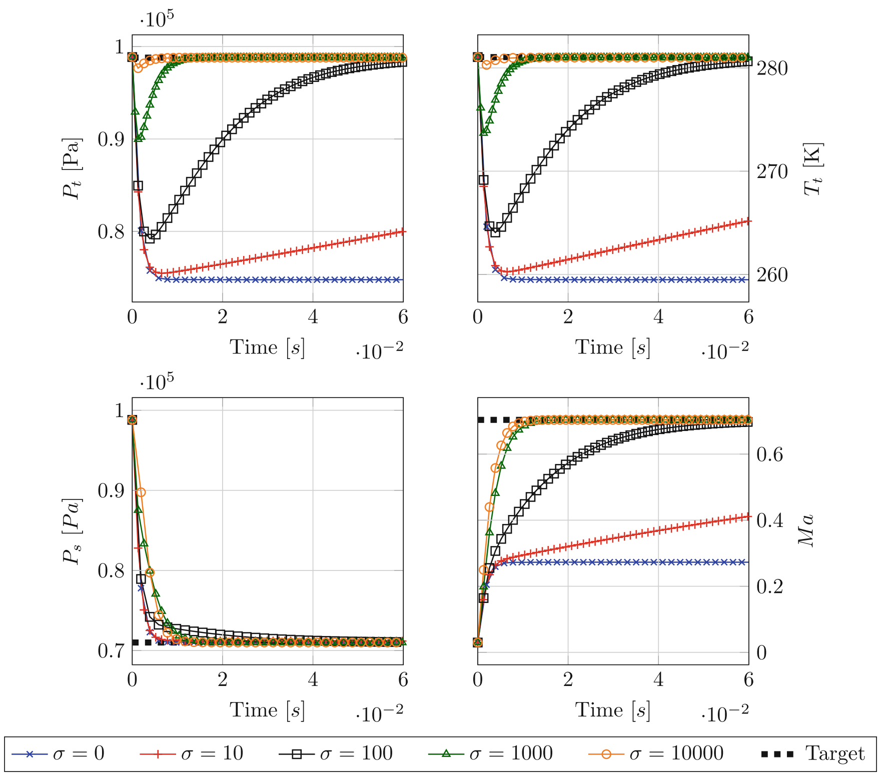

FIGURE 6 Convergence of the macroscopic values toward the imposed value with the $P_t - T_t$ inlet [Colour figure can be viewed at wileyonlinelibrary.com]

Considering the chosen physical values and the periodicity, the Mach number must reach the expected value of (with $\gamma = 1.4$):

$$Ma = \sqrt{\frac{2}{\gamma - 1}\left[\left(\frac{P_t}{P_s}\right)^{\frac{\gamma-1}{\gamma}} - 1\right]} = 0.7036. \tag{100}$$

The initial solution corresponds to a static pressure field and a static temperature field such that $P_s = P_t$ and $T_s = T_t$. As the fluid is considered a perfect gas, the density ρ is set such as $\rho = \frac{P_t}{rT_t}$. The initial velocity is set to $u_x = 10$ m s^{-1}. The initialization is deliberately chosen far from the converged solution to validate the capability to reach the target. All relaxation coefficients are equal in the following. To study the temporal evolution of P_t and T_t, a probe is located at the inlet boundary and the results are presented in Figure 6.

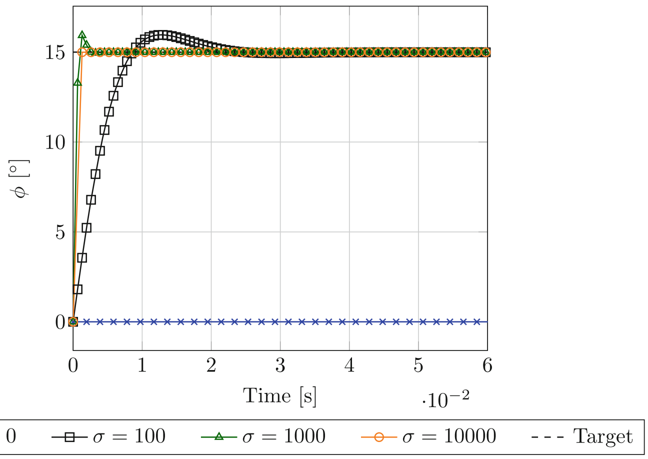

FIGURE 7 Convergence of the flow direction [Colour figure can be viewed at wileyonlinelibrary.com]

From the presented results, it is seen that the total quantities converge toward the imposed value for $\sigma \geq 100$. If the relaxation parameter chosen is too low, the simulation is not able to recover the desired solution. Moreover, the higher the relaxation parameter, the faster the convergence. Because of the periodic configuration, no loss occurs and the flow can be considered isentropic. This implies that the static pressure in the domain must be equal to the prescribed outlet static pressure.

4.2 | Flow direction validation

In the second test case, a flow direction is added by introducing an angle $\phi = 15°$ to the flow established in the previous test case. It is then possible to follow the convergence of the flow angle to the desired value depending on the value of the relaxation coefficient as illustrated in Figure 7.

Once again, it can be seen that a minimum value of the relaxation coefficient is needed to reach the target value and that a higher value of σ allows a faster convergence.

4.3 | Imposition of several Mach numbers

This section aims at validating the approach for a given range of inlet Mach numbers typically encountered in turbomachinery simulations.

Figure 8 shows that it is possible to go through all the desired Mach values inferior to 1. If the set-up results in a supersonic case, the Mach number converges and stays at 1. Indeed, for the supersonic case, the five waves are entering the domain, and the NSCBC approach specifying one outgoing and four incoming waves is no longer valid. For all Mach numbers, the relaxation coefficient used for the computation was $\sigma = 10^4$.

4.4 | Evaluation of the acoustic properties

The goal of this section is to evaluate the acoustic reflectivity of the proposed inlet boundary, for several values of the relaxation coefficient σ. The set up is the following: a left-going acoustic wave with a Gaussian shape is super-imposed to the flow established in the 2D-square box test case (Figure 9). The perturbation is initially centered at $x_0 = \frac{x}{L_x} = 0.75$ and the perturbation is defined as:

$$p' = -\rho c A \exp^{-\frac{(x-x_0)^2}{\Gamma^2}}, \tag{101}$$

with the perturbation amplitude $A = 0.001$ and $\Gamma = 0.01$.

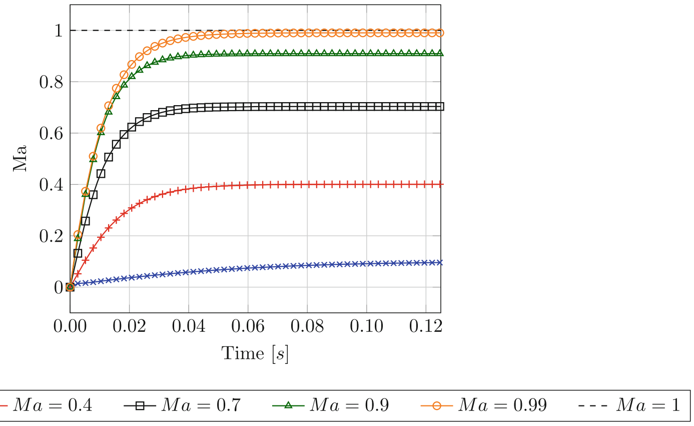

FIGURE 8 Convergence toward all the specified Mach numbers [Colour figure can be viewed at wileyonlinelibrary.com]

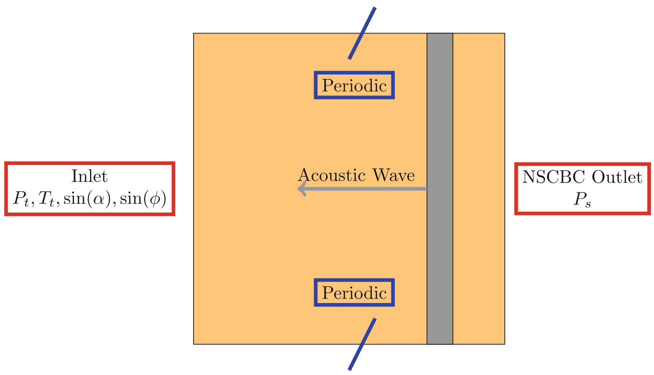

FIGURE 9 Scheme of the 2D-square box with the added acoustic wave [Colour figure can be viewed at wileyonlinelibrary.com]

Figure 10 illustrates pressure and velocity fluctuation evolution as the acoustic wave crosses the inlet boundary for several values of σ.

It can be seen that for a higher value of the relaxation coefficient, the intensity of the fluctuations on the velocity and pressure increases.

The reflection coefficient R is then evaluated from the pressure, velocity and density signals recorded at the inlet probe and decomposed into mean and fluctuating components such as:

$$p(t) = \tilde{p} + p'(t), \tag{102}$$

$$u(t) = \tilde{u} + u'(t), \tag{103}$$

$$\rho(t) = \tilde{\rho} + \rho'(t). \tag{104}$$

From these definitions, the inward and backward acoustic waves w_+ and w_- are computed using:

$$\begin{cases} w_+ = p' + \rho c u', & (105) \\ w_- = p' - \rho c u'. & (106) \end{cases}$$

Figure 11 shows the reflection coefficient R as well as the reconstructed waves w_+ at the inlet for several σ.

It illustrates that the relaxation coefficient is linked to the intensity of the reflection. Moreover, concerning the wave amplitude evolution, w_- should be present as it represents the Gaussian left going acoustic wave, but any value of w_+ is a sign of reflection, whose amplitude rises proportionally to σ.

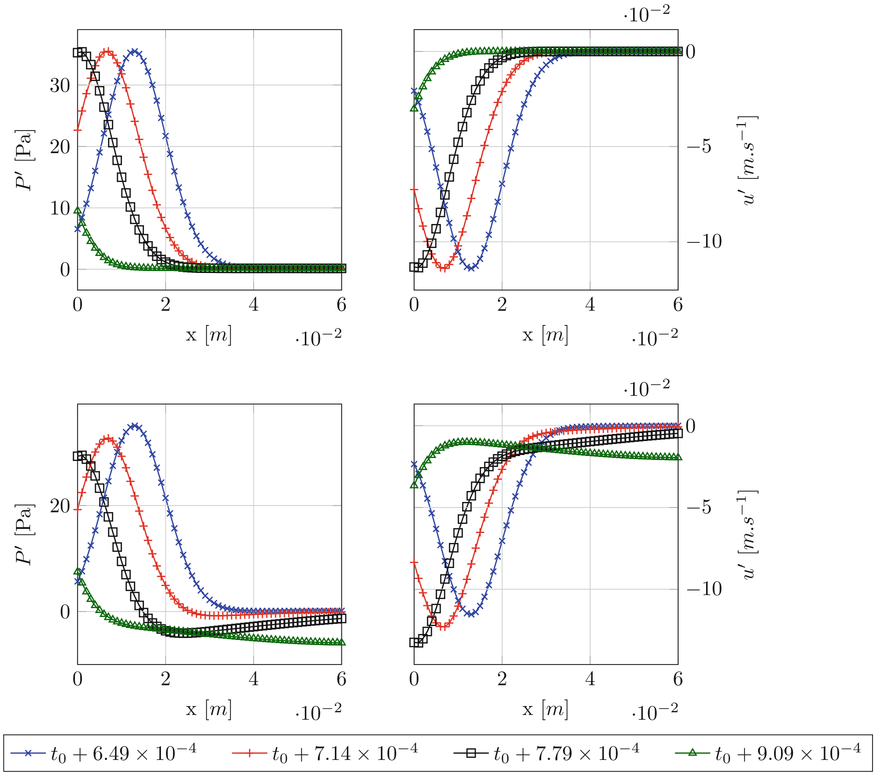

FIGURE 10 Pressure and velocity fluctuations at the inlet for $\sigma = 0$ (top) and $\sigma = 10^5$ (bottom) [Colour figure can be viewed at wileyonlinelibrary.com]

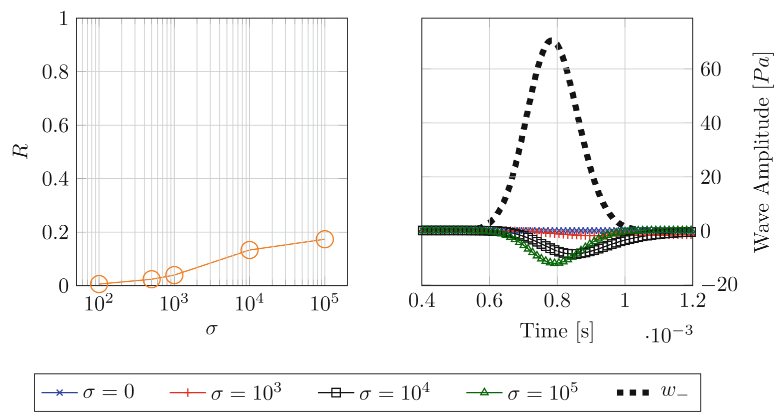

FIGURE 11 Plot of the reflection coefficient and acoustic waves [Colour figure can be viewed at wileyonlinelibrary.com]

4.5 | Synthetic turbulence injection

The three unsteady velocity components (u'_n, u'_{t1}, u'_{t2}) at the inlet are specified using a Kraichnan's approach.[67] Following the characteristic boundary condition proposed by Guézennec and Poinsot,[64] these fluctuations are added to the inlet acoustic wave $\mathcal{L}_+$ and the two transverse shear waves $\mathcal{L}_{t1}, \mathcal{L}_{t2}$ derived in Section 3 such that:

$$\mathcal{L}_{+,\text{turb}} = \mathcal{L}_+ + \frac{\partial u'_n}{\partial t}, \tag{107}$$

$$\mathcal{L}_{t_1,\text{turb}} = \mathcal{L}_{t_1} + \frac{\partial u'_{t_1}}{\partial t}, \tag{108}$$

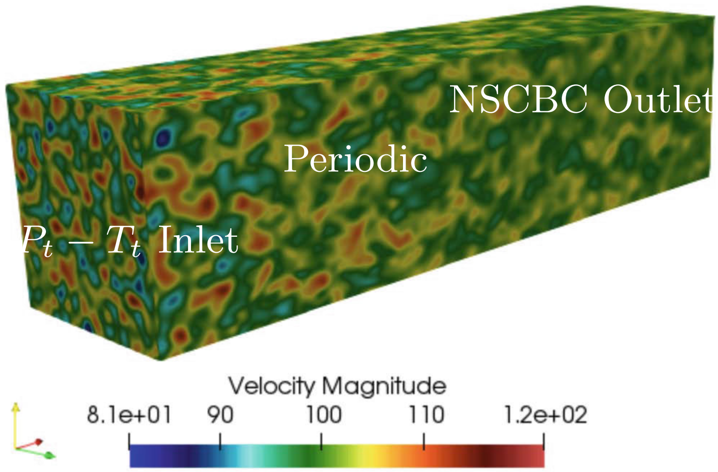

FIGURE 12 Illustration of the computational domain for the three-dimensional turbulent channel [Colour figure can be viewed at wileyonlinelibrary.com]

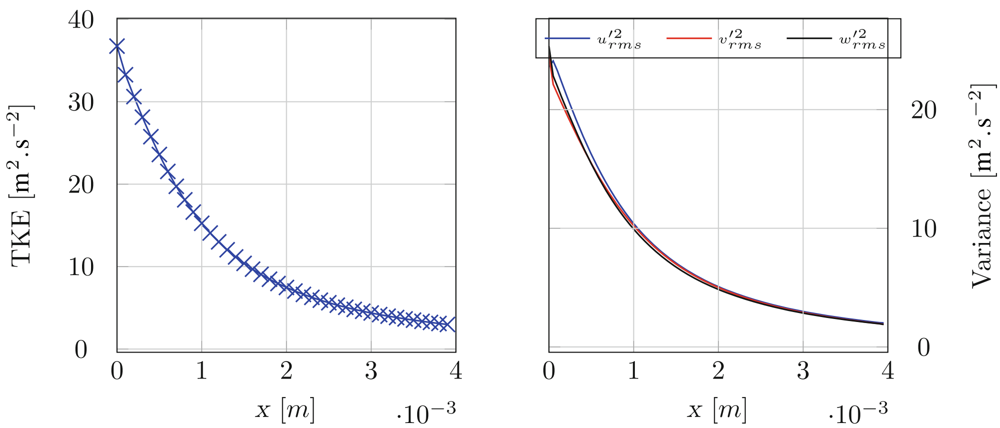

FIGURE 13 Plot of the turbulent kinetic energy and the RMS evolution along the domain [Colour figure can be viewed at wileyonlinelibrary.com]

$$\mathcal{L}_{t_2,\text{turb}} = \mathcal{L}_{t_2} + \frac{\partial u'_{t_2}}{\partial t}. \tag{109}$$

The proposed test case to validate the turbulence injection is a turbulent convected flow in a rectangular box. The computational domain is a rectangular box of dimensions $[L_x \times L_y \times L_z] = [4 \text{ mm} \times 1 \text{ mm} \times 1 \text{ mm}]$, discretized with $[n_x \times n_y \times n_z] = [392 \times 98 \times 98]$ cells (see Figure 12). The minimal mesh size of this test case imposes a time step $\Delta t = 1.7 \times 10^{-8}$ s. Total pressure and temperature P_t and T_t are imposed at the inlet, using a relaxation coefficient $\sigma = 10^4$, while static pressure P_s is imposed at the outlet so that the expected mean velocity is 100 m s^{-1}. All other boundaries are periodic conditions. The targeted turbulent kinetic energy is TKE = 37.5 m s^{-2}. Since the turbulent kinetic energy is given by TKE = $\frac{u'^2}{2}$, this leads to an inlet velocity fluctuation fixed as $u' = 5$ m s^{-1}. The target integral length-scale is $\lambda = \frac{\sqrt{2\pi}}{k_e} = \frac{\lambda_e}{\sqrt{2\pi}} = 0.56$ mm, with k_e the most energetic wave-number in the Passot–Pouquet spectrum, and λ_e the most energetic length-scale. We used 1000 modes to build the inlet velocity fluctuation field. Figure 12 shows the injection of vortical structures near the inlet.

Figure 13 shows the turbulent kinetic energy decrease expected within the domain. At the inlet, a value of $TKE = 37.5$ m s^{-2} is reached.

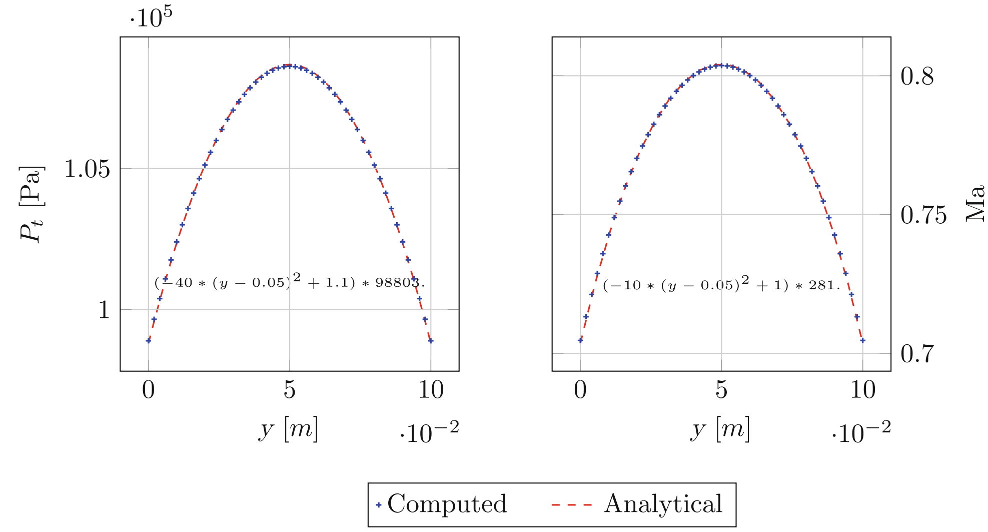

FIGURE 14 Illustration of the imposition of an inlet radial profile [Colour figure can be viewed at wileyonlinelibrary.com]

4.6 | Enforcing a radial profile for turbomachinery simulation

Typically, at the inlet of a turbomachinery simulation domain, radial profiles of quantities such as total pressure, total temperature and flow angles are imposed. It is thus necessary to ensure the capability of the boundary condition to correctly impose this kind of data. To do so, radial profiles of each macroscopic value are defined under the form of $Y = f(x, y, z)$ or $Y = f(x, r, \theta)$ with Y being P_t, T_t, ϕ, α, and f a polynomial function, dependent on the Cartesian or cylindrical coordinates.

For the radial profile, the expression of f is chosen such that:

- $P_t = (-40 * (y - y_0)^2 + 1.1) * P_{t,\text{mean}}$.
- $T_t = (-10 * (y - y_0)^2 + 1) * T_{t,\text{mean}}$.

These expressions are imposed on the inlet boundary of the 2D-square box test case defined in the first section using a relaxation coefficient $\sigma = 10^4$. The numerical and physical parameters are unchanged from the first 2D square box test case. Figure 14 illustrates that the inlet boundary condition properly produces total pressure and Mach number fields that correspond to the imposed radial profile and outlet static pressure of $P_s = 7.1 \times 10^4$ Pa.

4.7 | Partial conclusion

From the different test cases conducted in this section, several conclusions concerning the choice of the relaxation parameter can be drawn. From the first test case, it can be seen that the recommended range for the relaxation parameter is between 1000 and 10,000. These values allow to correctly converge toward the target in a reasonable physical time while keeping a low reflectivity. Choosing a value higher than 10^4 may also lead in some cases to stability issues. Moreover, at the end of this section, it has been illustrated that uniform values or radial profiles of P_t, T_t, α, and ϕ, with or without turbulence injection can be imposed at the inlet.

5 | STUDY OF THE RADIAL EQUILIBRIUM AT THE OUTLET

The usual method, used in RANS simulations, is to impose an outlet pressure profile consistent with the radial equilibrium. This approach leads to a fully reflecting outlet for acoustic waves. It is not an issue for RANS simulations, which do not capture the acoustics. However, it becomes an issue for LES. To overcome this problem, NSCBC are commonly used. For an outlet, they allow the user to control the influence of the incoming information through the manipulation of wave amplitudes. The study focuses on the investigation of how NSCBC conditions perform for flows with strong rotation. It is illustrated that the NSCBC formalism can let the physical radial pressure gradient establish naturally so that this formalism can be used at the outlet of turbomachinery simulations without additional treatment. This methodology has already been successfully applied within a standard LES solver AVBP.[29] The pursue of this study is to evaluate if it is reproducible in the LBM approach.

5.1 | Simplified radial equilibrium

The radial equilibrium equations were first derived in the 1940s–1950s.[68] It was shown that the whirling motion of a fluid inside a turbomachine creates a centrifugal force that has to be balanced by a centripetal one, thus creating a positive radial pressure gradient. This simplified radial equilibrium is obtained by considering a flow with the following properties:

- No viscous effects.
- Negligible heat conduction.
- A steady-state ($\frac{\partial}{\partial t} = 0$).
- No gravity or volumic forces.
- Axisymmetric flow ($\frac{\partial}{\partial \theta} = 0$).
- No radial velocity ($u_r = 0$).

Under these hypotheses, the flow is governed by the Euler equations for a compressible flow with the equation of state for an ideal gas. In cylindrical coordinates (r, θ, x), the momentum equation in the radial direction is

$$\frac{\partial u_r}{\partial t} + u_r \frac{\partial u_r}{\partial r} + \frac{u_\theta}{r}\frac{\partial u_r}{\partial \theta} - \frac{u_\theta^2}{r} + u_x \frac{\partial u_r}{\partial x} = -\frac{1}{\rho}\frac{\partial P}{\partial r}. \tag{110}$$

Applying the precedent assumptions to Equation (110) leads to the simplified radial equilibrium equation:

$$\frac{1}{\rho}\frac{\partial P}{\partial r} = \frac{u_\theta^2}{r}, \tag{111}$$

where P is the static pressure, u_θ is the azimuthal velocity component, and ρ is the density.

5.2 | Annulus test case

The test cases described below are presented in details in Koupper et al.[29] The ability of characteristic boundary conditions to recover the radial equilibrium assumption (REA) pressure profile is assessed in a rotating flow in a simple annulus, see Figure 15. The annulus has the following dimensions:

- $R_1 = 0.2$ m.
- $R_2 = 0.28$ m.
- $L = 0.32$ m.
- Aspect ratio: $\frac{L}{R_2 - R_1} = 4$.

This geometry is chosen because it produces an analytical solution, which can thus be used to validate the simulation.

5.2.1 | Analytical solution

The geometry and flow properties are set so that all hypotheses for the simplified radial equilibrium are fulfilled.

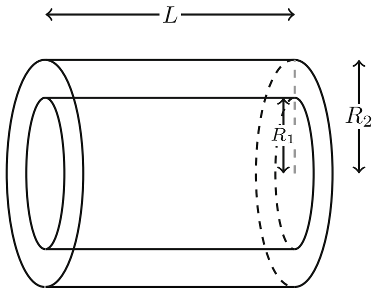

FIGURE 15 Geometry of the annulus test case

Two configurations are considered, namely the free vortex flow (FVF) (Equation 112) and the solid body rotation (SBR) (Equation 113). The radial pressure profile is obtained by integrating Equation (111) using the perfect gas relation to link density to pressure:

$$u_\theta = \frac{k}{r} \quad P(r) = \alpha_1 \exp\left(-\frac{k^2}{2r_{gas}T_s r^2}\right). \tag{112}$$

Or

$$u_\theta = C \quad P(r) = \alpha_2 r^{\left(\frac{C^2}{r_{gas*T_s}}\right)}. \tag{113}$$

α_1 and α_2 are integration constants that can be determined using the mean pressure on the outlet plane, $\overline{P_s}$.

$$\overline{P_s} = \frac{1}{A_{\text{annulus}}} \int\int P(r) r dr d\theta. \tag{114}$$

Solving Equation (114) for the two cases gives:

$$\alpha_1 = \frac{\overline{P_s}(R_2^2 - R_1^2)}{\left\{\left[\left(\frac{k^2}{2r_{gas}T}\right) Ei\left[\frac{-k^2}{2r_{gas}Tr^2}\right] + r^2 \exp\left[\frac{-k^2}{2r_{gas}Tr^2}\right]\right]\right\}_{R_1}^{R_2}}, \tag{115}$$

$$\begin{aligned}\frac{1}{A_{\text{annulus}}} \int\int P(r) r dr d\theta &= \frac{2\pi\alpha_2}{\pi(R_2^2 - R_1^2)} \int_{R_1}^{R_2} r^{\left(\frac{C^2}{r_{gas}T_s}\right)} \times r dr \\ &= \frac{2\alpha_2}{(R_2^2 - R_1^2)} \int_{R_1}^{R_2} r^{\left(\frac{C^2}{r_{gas}T_s}+1\right)} dr \\ &= \frac{2\alpha_2}{(R_2^2 - R_1^2)} \frac{\left[r^{\left(\frac{C^2}{r_{gas}T_s}+2\right)}\right]_{R_1}^{R_2}}{\frac{C^2}{r_{gas}T_s} + 2} \\ &= \overline{P_s}.\end{aligned}$$

It is then possible to isolate α_2:

$$\alpha_2 = \frac{\overline{P_s}(R_2^2 - R_1^2)\left(\frac{C^2}{r_{gas}T_s} + 2\right)}{2\left[r^{\left(\frac{C^2}{r_{gas}T_s}+2\right)}\right]_{R_1}^{R_2}}. \tag{116}$$

With the usual notation $[\phi(r)]_a^b = \phi(b) - \phi(a)$, $Ei(x)$ is the exponential integral function defined as $Ei(x) = \int_{-\infty}^{x} \frac{e^t}{t} dt$.

TABLE 1 Sum up of the parameters used during the simulations

Relaxation coefficient σ_{cbc} for FVF	2.52×10^{-4}	1.26×10^{-3}	6.30×10^{-3}	1.26×10^{-2}	1.26×10^{-1}
Relaxation coefficient σ_{cbc} for SBM	2.43×10^{-4}	1.21×10^{-3}	6.06×10^{-3}	1.21×10^{-2}	1.21×10^{-1}
$K_{cbc} = \frac{\sigma_{cbc}(1-Ma^2)c}{R_2-R_1}$	1	5	25	50	500
Flow through times FVF	0.76	0.76	0.64	0.42	0.42
Flow through times SBR	4.11	4.11	2.25	1.8	0.91

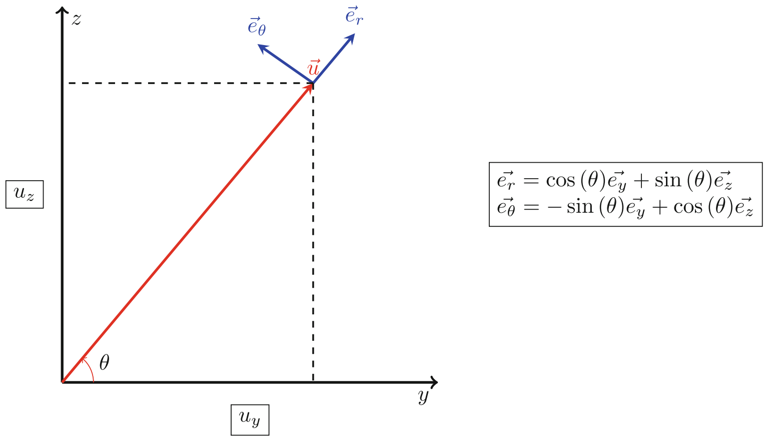

FIGURE 16 Plot of cylindrical coordinates and projection into Cartesian [Colour figure can be viewed at wileyonlinelibrary.com]

The target pressure is $\overline{P_s} = 10^5$ Pa. The shape of the pressure profile, governed by radius-dependent terms, is controlled by gas properties and by swirl profile $u_\theta(r)$.

5.2.2 | Numerical resolution

The swirling flow is simulated for six values of the outlet reflection coefficient σ, ranging from 1 to 1000, to assess the influence of the level of reflectivity on the radial equilibrium pressure profile. The annulus geometry is discretized with 50 points in the radial direction and 200 in the longitudinal direction. This is equivalent to a mesh size $\Delta x = 1.6 \times 10^{-3}$ m and a time step $\Delta t = 2.66 \times 10^{-6}$ s. To be coherent with the inviscid assumption of the simplified radial equilibrium, the physical behavior of the Euler equations is retrieved by setting the viscosity to zero. The summary of the test cases can be found in Table 1.

The inlet boundary condition imposes the adequate swirl profile $u_\theta(r)$ by imposing the corresponding total pressure and azimuthal angle. The axial velocity is set to $u_x = 5$ m s^{-1} for the FVF case or $u_x = 30$ m s^{-1} for the SBR one. The corresponding flow through times is noted τ and defined as $\tau = \frac{L}{u_x}$. The maximum Mach number during the computation is 0.29 for the FVF case while it is 0.17 for the SBR. The initial velocity field in the annulus is identical to the inlet boundary condition velocity profiles u_x, u_θ. At the outlet, the NSCBC 3D boundary condition is used with an imposed pressure $\overline{P_s}$. The inner and outer walls use slip conditions to avoid any near-wall effect on the velocity profile and thus on the pressure distribution. The initial pressure field is uniform such that $P(r, \theta, x) = \overline{P_s}$ and is thus not consistent with the REA to ensure that the NSCBCs are able to drive the pressure toward the REA.

To avoid using a rotational domain, the azimuthal velocity u_θ is specified in the Cartesian coordinates at the inlet according to (Figure 16):

$$u_y = -u_\theta \sin(\theta), \quad u_z = u_\theta \cos(\theta). \tag{117}$$

The required time to establish the pressure field is imposed by the domain size, flow properties, and relaxation parameter σ. Convergence is reached when the local pressure is $\pm 0.1\%$ of $P(t \to \infty)$. Increasing the relaxation parameter σ reduces

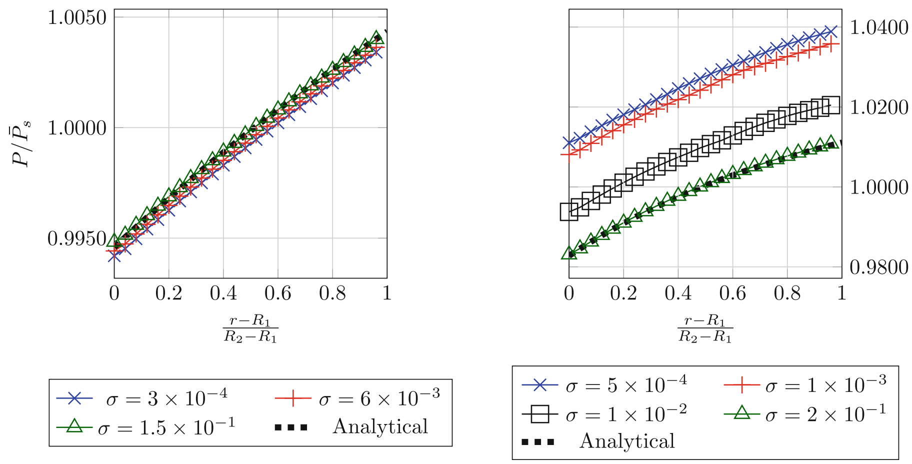

FIGURE 17 Results for the solid body rotation (left) and free vortex flow (right) [Colour figure can be viewed at wileyonlinelibrary.com]

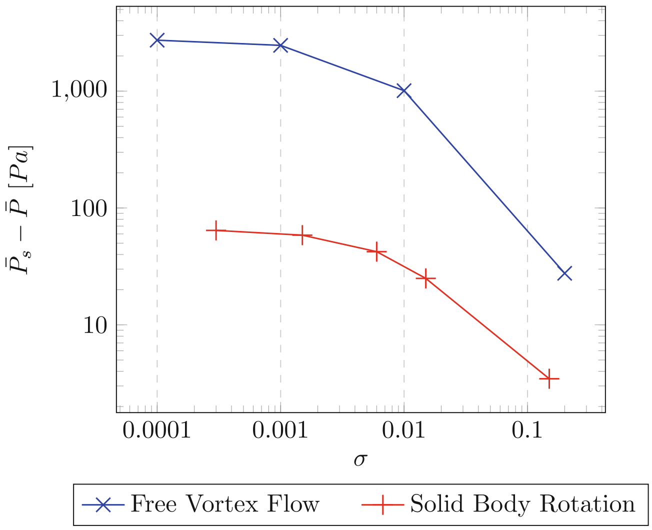

FIGURE 18 Illustration of the convergence toward the target pressure with increasing relaxation parameter σ [Colour figure can be viewed at wileyonlinelibrary.com]

the convergence time. As the pressure profile is only radius dependent (one-dimensional flow), it can be plotted at the domain exit. The simulations converge toward the theoretical profile as the relaxation coefficient at the outlet is increased. The main action of the relaxation coefficient σ is to drive the mean pressure toward the target. For $\sigma \rightarrow \infty$, the mean pressure would converge to the imposed value, and thus the pressure profile would exactly match the theoretical one. However, in this case, the boundary would become fully reflecting. The pressure profile is plotted at the domain exit in Figure 17. It can be seen that a radial equilibrium pressure profile establishes at the end of the simulation and that the profiles converge toward the analytical profile as the relaxation parameter at the outlet increased.

The role of the relaxation coefficient is, as explained before, to drive the static pressure toward the target. The reduction of the offset between the mean pressure and the target when increasing σ is illustrated in Figure 18. It can be seen that the error is inversely proportional to σ.

5.3 | Partial conclusion

In this section, it has been demonstrated that the NSCBC formalism applied on an outlet is compatible with strongly rotating flows usually found in turbomachinery. Concerning the choice of the relaxation coefficient, it should be noted

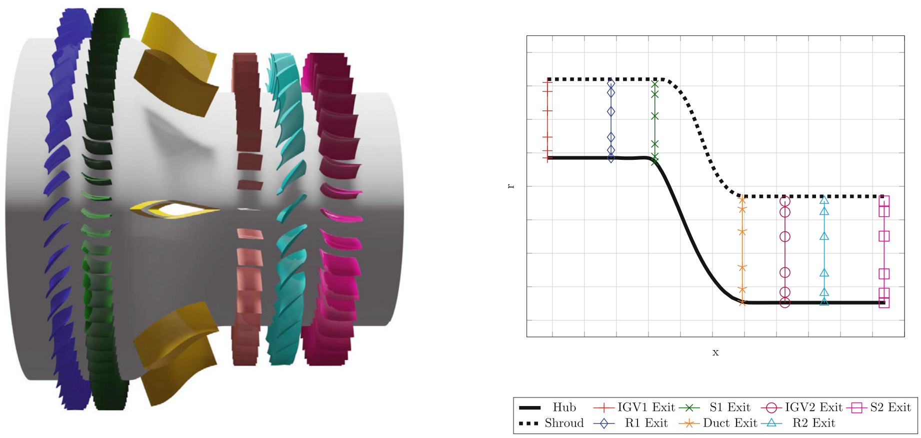

(A) (B)

FIGURE 19 Complete CAM1 geometry (left) and sketch of the computational domain (right) [Colour figure can be viewed at wileyonlinelibrary.com]

that a value around 0.2 leads to a pressure profile at the outlet close to the one predicted by the theory. The relaxation coefficient could be increased further to improve the precision of the results but this would lead to a fully reflective outlet which may have to be avoided.

6 | S-DUCT CONFIGURATION

The S-duct configuration illustrated in this section is taken from the European project AIDA and corresponds to the CAM1 geometry. The full configuration consists of a strutted S-duct located between a low-pressure compressor (LPC) and a high-pressure compressor (HPC) (see Figure 19A). For simplicity and because the goal here is simply to validate the correct application of the $P_t - T_t$ inlet boundary as well as the P_s at the outlet boundary, the computational domain is restricted to the strutted duct and the following inlet guide vane IGV2 (see Figure 19B).

6.1 | Initial and boundary conditions

The initial condition consists in a uniform field with no velocity and a static pressure corresponding to the one imposed at the outlet. The fluid considered is air with a kinematic viscosity at this temperature of 1.49×10^{-5} m^2 s^{-1}.

The total pressure, total temperature as well as the flow angles are imposed at the inlet by computing a polynomial interpolation from the experimental data available. This allows to impose a radial profile of these macroscopic quantities at the S1 exit plane with a relaxation coefficient fixed at 10^4. Moreover, turbulence is injected at the inlet with a velocity fluctuation $u' = 5$ m s^{-1}. At the outlet, situated one chord away from the IGV2 exit, static pressure is imposed using an NSCBC condition with a relaxation coefficient $\sigma = 0.25$.

6.2 | Wall law and SGS model

For this computation a wall law derived from the classical formulation but taking into account curvature, pressure gradient and near-wall damping is applied. Moreover, the shear-improved Smagorinsky model (SISM) is used with a standard Smagorinsky constant $C_s = 0.18$. These two methods have already been successfully applied with the LBM on complex configurations.[69,70]

6.3 | Meshing strategy

The Cartesian mesh is generated by specifying a minimal mesh size of 2.5×10^{-4} m applied on the walls while a maximal mesh size of 1×10^{-3} m is set in the rest of the simulation domain. This leads to a y^+ value of approximately 25 on the

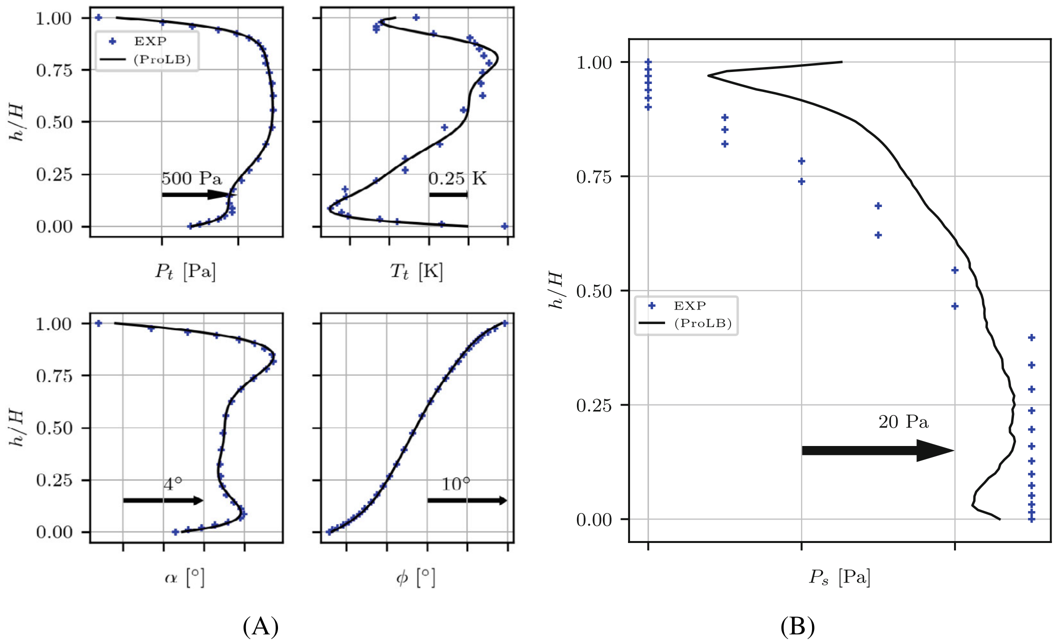

FIGURE 20 Plot of the inlet radial profiles (left) and check of the radial equilibrium assumption at the outlet [Colour figure can be viewed at wileyonlinelibrary.com]

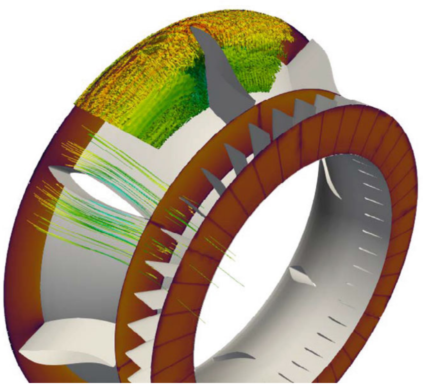

FIGURE 21 Contour of Q-criterion colored by vorticity and 2D map of Mach number at the different control planes [Colour figure can be viewed at wileyonlinelibrary.com]

walls which is in agreement with the recommendations in the literature[70] for the use of wall law. This leads to a mesh containing 250×10^6 equivalent fine cells. The corresponding time step for this computation is set by the smallest mesh size and is equal to $\Delta t = 1.7 \times 10^{-6}$ s.

6.4 | Results

Firstly, the mass-flow convergence was evaluated to check that the correct design point is reached. The difference between the computed mass-flow and the design one is 1% which is judged acceptable to compare the results in the following.

The radial profiles obtained at the inlet by azimuthal averaging are represented in Figure 20A while the radial evolution of the static pressure at the outlet is represented in Figure 21. It shows that the inlet imposes the desired values while the radial equilibrium is closely respected at the outlet. Finally, the flow field is depicted in more details in Figure 20B. It shows contours of Q-criterion colored by vorticity between the inlet and the strut to illustrate the turbulence injection as well as the averaged Mach number at the different control planes of the machine.

7 | CONCLUSIONS

Characteristic boundary conditions for compressible LBM simulations that impose total pressure P_t, total temperature T_t, and flow angles ϕ and α at the inlet and static pressure at the outlet verifying the radial equilibrium have been derived in this article. The compressible expressions of total pressure and total temperature are determined thanks to the NSCBC methodology so that it is expressed in terms of characteristic waves $\mathcal{L}_i$. The LODI relations and the imposed values of P_t, T_t, ϕ, α are then used to obtain the waves expressions $\mathcal{L}_i$. The formulation obtained has a behavior varying from non-reflecting to fully-reflecting, depending on the relaxation parameter used in the linear relaxation methodology.

The NSCBC formulation is assessed on several test cases with increasing complexity, for a broad range of relaxation coefficients. Results show that the values of the relaxation coefficients used enable to recover non-drifting mean values as well as reflecting or non-reflecting behavior. The possibility to add synthetic turbulence injection is demonstrated on a periodic rectangular box before being used on a turbomachinery simulation. The inlet boundary condition gives fair results regarding the expected turbulent kinetic energy.

Moreover, the REA at the outlet of the computational domain is validated considering the annulus test case. This assumption is of high importance in regards to turbomachinery simulations, and the capacity of the NSCBC to deal with the radial equilibrium and the control of acoustic waves must be assessed. Results show that low errors on the pressure profile are obtained even when using low values of the relaxation parameter σ thanks to characteristic boundary conditions taking into account transverse terms.

Finally, this boundary condition is applied for a turbomachinery configuration corresponding to an S-duct stage. The case of an S-duct simulation is illustrated here with the imposition of total quantities under the form of radial profiles. The test case shows the ability to recover the imposed target values, to handle radial profiles and turbulence injection at the inlet while simultaneously allowing the development of the radial profile of static pressure at the outlet. This paves the way for more complex turbomachinery simulations using the lattice Boltzmann method.

ACKNOWLEDGMENTS

The authors would like to thank Safran Aircraft Engines and ANRT/CIFRE Convention No. 2019/1448 for their financial support, as well as for access to high performance computing resources. This work has been carried out using ProLB, a lattice-Boltzmann solver currently being developed by a consortium including CS Group, Airbus, Renault, Aix-Marseille Université, and École Centrale Lyon.

CONFLICT OF INTEREST

The authors declare no potential conflict of interest.

DATA AVAILABILITY STATEMENT

The data that support the findings of this study are available from the corresponding author upon reasonable request.

ORCID

Thomas Gianoli https://orcid.org/0000-0002-1516-3422
Jérôme de Laborderie https://orcid.org/0000-0003-3678-8648

REFERENCES

1. Qian YH, D'Humières D, Lallemand P. Lattice BGK models for Navier-Stokes equation. *Eplasty*. 1992;17(6):479-484. doi:10.1209/0295-5075/17/6/001
2. Kruger T, Kusumaatmaja H, Kuzmin A, Shardt O, Goncalo S, Viggen EM. *The Lattice Boltzmann Method: Principles and Practice*. Vol 207. Springer; 2017.
3. Girimaji S. Lattice Boltzmann method: fundamentals and engineering applications with computer codes. *AIAA J*. 2013;51(1):278-279.
4. Feng ZG, Michaelides EE. The immersed boundary-lattice Boltzmann method for solving fluid-particles interaction problems. *J Comput Phys*. 2004;195(2):602-628. doi:10.1016/j.jcp.2003.10.013
5. Krüger T, Varnik F, Raabe D. Efficient and accurate simulations of deformable particles immersed in a fluid using a combined immersed boundary lattice Boltzmann finite element method. *Comput Math Appl*. 2011;61(12):3485-3505. doi:10.1016/j.camwa.2010.03.057

6. Favier J, Revell A, Pinelli A, et al. A lattice Boltzmann - immersed boundary method to simulate the fluid interaction with moving and slender flexible objects. *J Comput Phys*. 2014;261:145-161.
7. Chen GQ, Huang X, Zhang AM, Wang SP, Li T. Three-dimensional simulation of a rising bubble in the presence of spherical obstacles by the immersed boundary-lattice Boltzmann method. *Phys Fluids*. 2019;31(9):5115097. doi:10.1063/1.5115097
8. Buick JM, Greated CA, Campbell DM. Lattice BGK simulation of sound waves. *Europhys Lett*. 1998;43(3):235-240. doi:10.1209/epl/i1998-00346-7
9. Marié S, Ricot D, Sagaut P. Comparison between lattice Boltzmann method and Navier-Stokes high order schemes for computational aeroacoustics. *J Comput Phys*. 2009;228(4):1056-1070. doi:10.1016/j.jcp.2008.10.021
10. Xu K, Liu C. A paradigm for modeling and computation of gas dynamics. *Phys Fluids*. 2017;29(2):1-17. doi:10.1063/1.4974873
11. Chen Y, Zhu Y, Xu K. A three-dimensional unified gas-kinetic wave-particle solver for flow computation in all regimes. *Phys Fluids*. 2020;32(9):0021199. doi:10.1063/5.0021199
12. Es-Sahli O, Sescu A, Afsar MZ, Buxton OR. Investigation of wakes generated by fractal plates in the compressible flow regime using large-eddy simulations. *Phys Fluids*. 2020;32(10):0018712. doi:10.1063/5.0018712
13. Astoul T, Wissocq G, Boussuge JF, Sengissen A, Sagaut P. Analysis and reduction of spurious noise generated at grid refinement interfaces with the lattice Boltzmann method. *J Comput Phys*. 2020;418:109645. doi:10.1016/j.jcp.2020.109645
14. Ma Y, Yang Z. Simplified and highly stable thermal Lattice Boltzmann method simulation of hybrid nanofluid thermal convection at high Rayleigh numbers. *Phys Fluids*. 2020;32(1):5139092. doi:10.1063/1.5139092
15. Hosseini SA, Abdelsamie A, Darabiha N, Thévenin D. Low-mach hybrid lattice Boltzmann-finite difference solver for combustion in complex flows. *Phys Fluids*. 2020;32(7):1-13. doi:10.1063/5.0015034
16. Fei L, Du J, Luo KH, et al. Modeling realistic multiphase flows using a non-orthogonal multiple-relaxation-time lattice Boltzmann method. *Phys Fluids*. 2019;31(4):5087266. doi:10.1063/1.5087266
17. Feng Y, Sagaut P, Tao W. A three dimensional lattice model for thermal compressible flow on standard lattices. *J Comput Phys*. 2015;303(September):514-529. doi:10.1016/j.jcp.2015.09.011
18. Wilde D, Krämer A, Reith D, Foysi H. Semi-Lagrangian lattice Boltzmann method for compressible flows. *Phys Rev E*. 2020;101(5):053306. doi:10.1103/PhysRevE.101.053306
19. Saadat MH, Karlin IV. Arbitrary Lagrangian-Eulerian formulation of lattice Boltzmann model for compressible flows on unstructured moving meshes. *Phys Fluids*. 2020;32(4):46105-46156. doi:10.1063/5.0004024
20. Reyhanian E, Dorschner B, Karlin IV. Thermokinetic lattice Boltzmann model of nonideal fluids. *Phys Rev E*. 2020;102(2):020103. doi:10.1103/PhysRevE.102.020103
21. Renard F, Wissocq G, Boussuge JF, Sagaut P. A linear stability analysis of compressible hybrid lattice Boltzmann methods. *J Comput Phys*. 2021;446(2):110649. doi:10.1016/j.jcp.2021.110649
22. Lee K, Yu D, Girimaji SS. Lattice Boltzmann DNS of decaying compressible isotropic turbulence with temperature fluctuations. *Int J Comput Fluid Dyn*. 2006;20:401-413. doi:10.1080/10618560601001122
23. Lew PT, Lyrintzis A, Crouse B, Balasubramanian G, Freed D, Mongeau L. Noise prediction of a subsonic turbulent round jet using the lattice-Boltzmann method. Proceedings of the 13th AIAA/CEAS Aeroacoustics Conference (28th AIAA Aeroacoustics Conference); September 2007. doi:10.1121/1.3458846
24. Scagliarini A, Biferale L, Sbragaglia M, Sugiyama K, Toschi F. Lattice Boltzmann methods for thermal flows: continuum limit and applications to compressible Rayleigh-Taylor systems. *Phys Fluids*. 2010;22(5):1-21. doi:10.1063/1.3392774
25. Begum R, Basit MA. Lattice Boltzmann method and its applications to fluid flow problems. *Eur J Sci Res*. 2008;22(2):216-231.
26. Poinsot TJ, Lele SK. Boundary conditions for direct simulations of compressible viscous flows. *J Comput Phys*. 1992;101(1):104-129. doi:10.1016/0021-9991(92)90046-2
27. Rakopoulos CD, Dimaratos AM, Giakoumis EG, Rakopoulos DC. Study of turbocharged diesel engine operation, pollutant emissions and combustion noise radiation during starting with bio-diesel or N-butanol diesel fuel blends. *Appl Energy*. 2011;88(11):3905-3916. doi:10.1016/j.apenergy.2011.03.051
28. Daviller G, Oztarlik G, Poinsot T. A generalized non-reflecting inlet boundary condition for steady and forced compressible flows with injection of vortical and acoustic waves. *Comput Fluids*. 2019;190(June 2019):503-513. doi:10.1016/j.compfluid.2019.06.027
29. Koupper C, Poinsot T, Gicquel L, Duchaine F. Compatibility of characteristic boundary conditions with radial equilibrium in turbomachinery simulations. *AIAA J*. 2014;52(12):2829-2839. doi:10.2514/1.J052915
30. Odier N, Sanjosé M, Gicquel L, Poinsot T, Moreau S, Duchaine F. A characteristic inlet boundary condition for compressible, turbulent, multispecies turbomachinery flows. *Comput Fluids*. 2019;178:41-55. doi:10.1016/j.compfluid.2018.09.014
31. Carullo JS, Nasir S, Cress RD, et al. The effects of freestream turbulence, turbulence length scale, and exit reynolds number on turbine blade heat transfer in a transonic cascade. *J Turbomach*. 2011;133(1):1-11. doi:10.1115/1.4001366
32. Jahanmiri M. *Boundary Layer Transitional Flow in Gas Turbines*. Chalmers University of Technology; 2011:1-51.
33. Collado Morata E, Gourdain N, Duchaine F, Gicquel LY. Effects of free-stream turbulence on high pressure turbine blade heat transfer predicted by structured and unstructured les. *Int J Heat Mass Transf*. 2012;55(21-22):5754-5768. doi:10.1016/j.ijheatmasstransfer.2012.05.072
34. Wissink JG, Zaki TA, Rodi W, Durbin PA. The effect of wake turbulence intensity on transition in a compressor cascade. *Flow Turbul Comb*. 2014;93(4):555-576. doi:10.1007/s10494-014-9559-z
35. Michelassi V, Chen LW, Pichler R, Sandberg RD. Compressible direct numerical simulation of low-pressure turbines: Part II—Effect of inflow disturbances. *Turbo Expo: Power for Land, Sea, and Air*. Vol 45639. American Society of Mechanical Engineers; 2014:V02DT44A014.

36. Scillitoe AD, Tucker PG, Adami P. Numerical investigation of three-dimensional separation in an axial flow compressor: the influence of free-stream turbulence intensity and Endwall boundary layer state. *Proc ASME Turbo Expo*. 2020;2016:57241. doi:10.1115/GT2016-57241
37. Wissocq G, Gourdain N, Malaspinas O, Eyssartier A. Regularized characteristic boundary conditions for the Lattice-Boltzmann methods at high Reynolds number flows. *J Comput Phys*. 2017;331:1-18. doi:10.1016/j.jcp.2016.11.037
38. Feng Y, Guo S, Jacob J, Sagaut P. Solid wall and open boundary conditions in hybrid recursive regularized lattice Boltzmann method for compressible flows. *Phys Fluids*. 2019;31(12):5129138. doi:10.1063/1.5129138
39. Shan X, Yuan XF, Chen H. Kinetic theory representation of hydrodynamics: a way beyond the Navier-Stokes equation. *J Fluid Mech*. 2006;550(August 2017):413-441. doi:10.1017/S0022112005008153
40. Luo LS, Liao W, Chen X, Peng Y, Zhang W. Numerics of the lattice Boltzmann method: effects of collision models on the lattice Boltzmann simulations. *Phys Rev E Stat Nonlinear Soft Matter Phys*. 2011;83(5):56710-56734. doi:10.1103/PhysRevE.83.056710
41. Mohamad AA. *Lattice Boltzmann Method*. Springer Science and Business Media; 2011.
42. Zhaoli Guo CS. *Lattice Boltzmann Method and Its Applications in Engineering*. World Scientific; 2013.
43. Lallemand P, Luo LS. Theory of the lattice Boltzmann method: acoustic and thermal properties in two and three dimensions. *Phys Rev E Stat Phys Plasmas Fluids Relat Interdiscip Top*. 2003;68(3):25. doi:10.1103/PhysRevE.68.036706
44. Malaspinas O. Increasing stability and accuracy of the lattice Boltzmann scheme: recursivity and regularization. arXiv preprint arXiv:1505.06900; 2015:1-31.
45. Siebert DN, Hegele LA, Philippi PC. Lattice Boltzmann equation linear stability analysis: thermal and athermal models. *Phys Rev E Stat Nonlinear Soft Matter Phys*. 2008;77(2):26707-25716. doi:10.1103/PhysRevE.77.026707
46. Farag G, Zhao S, Coratger T, Boivin P, Chiavassa G, Sagaut P. A pressure-based regularized lattice-Boltzmann method for the simulation of compressible flows. *Phys Fluids*. 2020;32(6):0011839. doi:10.1063/5.0011839
47. Jacob J, Malaspinas O, Sagaut P. A new hybrid recursive regularised Bhatnagar–Gross–Krook collision model for lattice Boltzmann method-based large eddy simulation. *J Turbul*. 2019;19(11):1051-1076. doi:10.1080/14685248.2018.1540879
48. Feng YL, Guo SL, Tao WQ, Sagaut P. Regularized thermal lattice Boltzmann method for natural convection with large temperature differences. *Int J Heat Mass Transf*. 2018;125:1379-1391. doi:10.1016/j.ijheatmasstransfer.2018.05.051
49. Feng Y, Boivin P, Jacob J, Sagaut P. Hybrid recursive regularized lattice Boltzmann simulation of humid air with application to meteorological flows. *Phys Rev E*. 2019;100(2):023304. doi:10.1103/PhysRevE.100.023304
50. Feng Y, Boivin P, Jacob J, Sagaut P. Hybrid recursive regularized thermal lattice Boltzmann model for high subsonic compressible flows. *J Comput Phys*. 2019;394:82-99. doi:10.1016/j.jcp.2019.05.031
51. Guo S, Feng Y, Jacob J, Renard F, Sagaut P. An efficient lattice Boltzmann method for compressible aerodynamics on D3Q19 lattice. *J Comput Phys*. 2020;418(May):109570. doi:10.1016/j.jcp.2020.109570
52. Guo S, Feng Y, Sagaut P. Improved standard thermal lattice Boltzmann model with hybrid recursive regularization for compressible laminar and turbulent flows. *Phys Fluids*. 2020;32(12):0033364. doi:10.1063/5.0033364
53. Farag G, Coratger T, Wissocq G, Zhao S, Boivin P, Sagaut P. A unified hybrid lattice-Boltzmann method for compressible flows: bridging between pressure-based and density-based methods. *Phys Fluids*. 2021;33(8):0057407. doi:10.1063/5.0057407
54. Bauer M, Silva G, Rüde U. Truncation errors of the D3Q19 lattice model for the lattice Boltzmann method. *J Comput Phys*. 2020;405:109111. doi:10.1016/j.jcp.2019.109111
55. Nguyen M, Boussuge JF, Sagaut P, Larroya-Huguet JC. Large eddy simulation of a thermal impinging jet using the lattice Boltzmann method. *Phys Fluids*. 2022;34(5):055115. doi:10.1063/5.0088410
56. Kim KH, Kim C, Rho OH. Methods for the accurate computations of hypersonic flows. II. Shock-aligned grid technique. *J Comput Phys*. 2001;174(1):81-119. doi:10.1006/jcph.2001.6896
57. Wrobel L. *Numerical Computation of Internal and External Flows. Volume 2: Computational Methods for Inviscid and Viscous Flows*. Vol 9. Elsevier Science; 1992.
58. Izquierdo S, Fueyo N. Characteristic nonreflecting boundary conditions for open boundaries in lattice Boltzmann methods. *Phys Rev E Stat Nonlinear Soft Matter Phys*. 2008;78(4):1-7. doi:10.1103/PhysRevE.78.046707
59. Heubes D, Bartel A, Ehrhardt M. Characteristic boundary conditions in the lattice Boltzmann method for fluid and gas dynamics. *J Comput Appl Math*. 2014;262:51-61. doi:10.1016/j.cam.2013.09.019
60. Latt J, Chopard B. Lattice Boltzmann method with regularized pre-collision distribution functions. *Math Comput Simul*. 2006;72(2-6):165-168. doi:10.1016/j.matcom.2006.05.017
61. Malaspinas O, Chopard B, Latt J. General regularized boundary condition for multi-speed lattice Boltzmann models. *Comput Fluids*. 2011;49(1):29-35. doi:10.1016/j.compfluid.2011.04.010
62. Latt J, Chopard B, Malaspinas O, Deville M, Michler A. Straight velocity boundaries in the lattice Boltzmann method. *Phys Rev E Stat Nonlinear Soft Matter Phys*. 2008;77(5);29-35. doi:10.1103/PhysRevE.77.056703
63. Thompson KW. Time dependent boundary conditions for hyperbolic systems. *J Comput Phys*. 1987;68(1):1-24. doi:10.1016/0021-9991(87)90041-6
64. Guézennec N, Poinsot T. Acoustically nonreflecting and reflecting boundary conditions for vorticity injection in compressible solvers. *AIAA J*. 2009;47(7):1709-1722. doi:10.2514/1.41749
65. Pirozzoli S, Colonius T. Generalized characteristic relaxation boundary conditions for unsteady compressible flow simulations. *J Comput Phys*. 2013;248:109-126. doi:10.1016/j.jcp.2013.04.021
66. Selle L, Nicoud F, Poinsot T. Actual impedance of nonreflecting boundary conditions: implications for computation of resonators. *AIAA J*. 2004;42(5):958-964.

67. Kraichnan RH. Diffusion by a random velocity field. *Phys Fluids*. 1970;13(1):22-31. doi:10.1063/1.1692799
68. Smith J. The radial-equilibrium equation of turbomachinery. *J Eng Power*. 1966;88(1):1-12. doi:10.1115/1.3678471
69. Leveque E, Touil H, Malik S, Ricot D, Sengissen A. Wall-modeled large-eddy simulation of the flow past a rod-airfoil tandem by the lattice Boltzmann method. *Int J Numer Methods Heat Fluid Flow*. 2018;28(5):1096-1116. doi:10.1108/HFF-06-2017-0258
70. Boudet J, Lévêque E, Touil H. Unsteady lattice Boltzmann simulations of corner separation in a compressor cascade. *J Turbomach*. 2022;144(1):1-12. doi:10.1115/1.4052017

How to cite this article: Gianoli T, Boussuge J-F, Sagaut P, de Laborderie J. Development and validation of Navier–Stokes characteristic boundary conditions applied to turbomachinery simulations using the lattice Boltzmann method. *Int J Numer Meth Fluids*. 2023;95(4):528-556. doi: 10.1002/fld.5160